

2015

DESIGNING A BIOSENSING DEVICE BASED ON WAVELENGTH SELECTIVE EMITTERS

Fabian Liebscher
University of Rhode Island, fliebscher@my.uri.edu

Follow this and additional works at: <https://digitalcommons.uri.edu/theses>

Terms of Use

All rights reserved under copyright.

Recommended Citation

Liebscher, Fabian, "DESIGNING A BIOSENSING DEVICE BASED ON WAVELENGTH SELECTIVE EMITTERS" (2015). *Open Access Master's Theses*. Paper 765.
<https://digitalcommons.uri.edu/theses/765>

This Thesis is brought to you by the University of Rhode Island. It has been accepted for inclusion in Open Access Master's Theses by an authorized administrator of DigitalCommons@URI. For more information, please contact digitalcommons-group@uri.edu. For permission to reuse copyrighted content, contact the author directly.

DESIGNING A BIOSENSING DEVICE BASED ON WAVELENGTH
SELECTIVE EMITTERS

BY

FABIAN LIEBSCHER

A MASTER THESIS SUBMITTED IN PARTIAL FULFILLMENT OF THE
REQUIREMENTS FOR THE DEGREE OF

MASTER OF SCIENCE

IN

INDUSTRIAL AND SYSTEMS ENGINEERING

UNIVERSITY OF RHODE ISLAND

2015

MASTER OF SCIENCE IN INDUSTRIAL AND SYSTEMS ENGINEERING
OF
FABIAN LIEBSCHER

APPROVED:

Thesis Committee:

Major Professor Yi Zheng

Hongyan Yuan

Kunal Mankodiya

Nasser H. Zawia
DEAN OF THE GRADUATE SCHOOL

UNIVERSITY OF RHODE ISLAND
2015

ABSTRACT

In this study, a new approach to design biosensors based on selective thermal emitters is developed. This approach allows the detection of biological molecules or chemical compounds in solution using the unique thermal emissivity spectra of each molecule. However in the last decades the applied and developed biosensors mainly use changes in electrical properties such as current or voltage or changes in optical characteristics caused by surface Plasmon resonance or fluorescence. After years of research, these sensors still show disadvantages such as high cost and time-consumptions. Biosensors based on selective thermal emitter provide an opportunity to avoid these weaknesses while they show a high selectivity and sensitivity, if the emission spectrum matches with the analyte(s) of interest.

Therefore, various different designs of selective emitters are simulated. The physical principles of radiation heat transfer are transferred into a MATLAB code in order to analyze and compare the different emissivity spectra with certain molecules and chemical compounds. The investigated designs are thin film applications (single and multilayer) as well as polymers doped with nanoparticles. The needed optical properties, defined by the permittivity of the materials are implemented, as well. The results show that selective thermal emitter can serve as biosensors e.g. for DNA due to their unique spectrum of emissivity.

ACKNOWLEDGMENTS

This past year has been one of the most interesting and exciting years, both personally and professional and would not have been possible without the help of so many people on so many levels.

First of all, I would like to thank my Major Advisor, Prof. Yi Zheng, for his patience, encouragement, continuous help and advices throughout my thesis. Without him and his invaluable advices the research would not have been possible.

I would like to thank Prof. H. Sun and his team for fabricating the investigated samples and the insights in fabrication processes.

Thanks to the members of my committee: Prof. Yi Zheng, Prof. Hongyan Yuan and Prof. Kunal Mankodiya and my defense chair Prof. Xinyuan Chen. I am very grateful that they all accepted to review my work and thesis.

I feel grateful for everyone who has been a part of my studies and contributed to it in any possible way.

Finally I would like to thank my loving and supportive family. Thank you for always being there, whether I needed motivation or just a good laugh to relieve some stress.

TABLE OF CONTENTS

ABSTRACT	ii
ACKNOWLEDGMENTS	iii
TABLE OF CONTENTS	iv
LIST OF TABLES	vi
LIST OF FIGURES	vii
LIST OF ABBREVIATIONS	x
LIST OF SYMBOLS	xii
CHAPTER 1 – INTRODUCTION	1
CHAPTER 2 – REVIEW OF LITERATURE	3
2.1. Biosensors	3
2.2. Categorization of Biosensors	5
2.2.1. Optical transducer	5
2.2.2. Electrochemical transducer	8
2.2.3. Piezoelectric biosensors	12
2.3. Selective thermal emitters and their application	13
2.3.1. Selective thermal emitters	13
2.3.2. Application in energy conversion systems (TPV).....	14
CHAPTER 3 – METHODOLOGY	16
3.1. Basic functionality	16
3.1.1. Design boundaries and constraints.....	20
3.2. Calculation of hemispherical emissivity	23
3.2.1. The wave vector k	25
3.2.2. Complex refractive index	27

3.2.3. Permittivity.....	28
3.2.4. Spectral hemispherical emissivity and refraction coefficient	32
3.3. Implementing in Matlab.....	34
3.4. Simulation and Validation of the introduced material groups	38
3.5. Selectivity of different chemical and biological molecules	45
CHAPTER 4 – Results.....	47
4.1. Hemispherical emissivity of various polar material structures	47
4.1.1. Thin film structures of polar materials	47
4.1.2. Doped polar material.....	49
4.2. PS doped with Au nanoparticles	53
4.3. Evaluation of Results	58
4.4. Experimental measurement.....	59
4.4.1. Fabrication of samples	60
4.4.2. Results FTIR spectroscopy.....	62
CHAPTER 5 – CONCLUSION.....	67
APPENDICES	69
BIBLIOGRAPHY	70

LIST OF TABLES

Table 1 Parameters and their values, which are needed in order to calculate the complex dielectric function of the polar materials SiC and BN [64].....	29
Table 2 Parameters and their values, which are needed in order to calculate the complex dielectric function of PS [66]	29
Table 3 Absorption wavelength of various molecule/materials at room temperature .	45
Table 4 Analyte and possible marker material.....	45

LIST OF FIGURES

Figure 1 Basic structure of biosensors consisting of a biological recognition element and a transducer, which is generating a signal that can be analyzed after electronic processing.....	3
Figure 2 Optical waveguide sensor - fabrication steps [35].....	7
Figure 3 The Fabrication of TiO ₂ nanotubes and the measurement process to detect glucose [39].....	9
Figure 4 The process steps in order to immobilize/synthesize the target DNA onto the Au electrode (GE) [2]	11
Figure 5 Various Photonic Crystal Designs, a) 1D, b) 2D, c) 3D.....	14
Figure 6 Functional structure of conventional TPV systems without selective thermal emitter [48].....	14
Figure 7 Examples of 2D [49] and 3D [50] photonic crystal designs.....	15
Figure 8 Basic principle of how a sample droplet on top of a selective thermal emitter influences the hemispherical emissivity.	17
Figure 9 The basic principle in order to quantify the sample in the visible/near-UV spectrum.....	19
Figure 10 Material groups of interest in this study: polar materials, polymers, doped polymer	21
Figure 11 Interaction of the in-plane wave vector k_i at an interface between two media/layer [56]	26

Figure 12 Reflection and Transmission for a multilayer stack of polar thin films	33
Figure 13 Flowchart of the self-written MATLAB-Code with its subscripts and for-loops	34
Figure 14 Real and Imaginary parts of the complex dielectric function of SiC	39
Figure 15 Hemispherical emissivity of SiC thin films on Au-coated substrate for various layer thickness	39
Figure 16 Hemispherical Emissivity of PS thin film on Au-coated substrate for a thickness of 0.4 μm	41
Figure 17 Real and imaginary parts of the complex dielectric function of Au.....	43
Figure 18 Hemispherical emissivity for PS thin films doped with Au-NPs of various volume fractions (0%, 5%, 10% and 30%).....	44
Figure 19 Hemispherical emissivity of BN thin films on Au-coated substrate for various layer thickness	48
Figure 20 Hemispherical emissivity for SiC thin films doped with BN-NPs of various volume fractions (10%, 20% and 30%)	49
Figure 21 Hemispherical emissivity for BN thin films doped with SiC-NPs of various volume fractions (10%, 20% and 30%)	51
Figure 22 Hemispherical emissivity for various combinations of SiC and BN.....	52
Figure 23 Hemispherical emissivity of a PS thin layer ($d=0.40 \mu\text{m}$) doped with various volume fractions of Au nanoparticles ($r=25 \text{ nm}$).....	53
Figure 24 Hemispherical emissivity of a Polystyrene layer doped with Au nanoparticles with various volume fraction from 0% to 25%	56

Figure 25 Hemispherical emissivity of a Polystyrene layer doped with Au nanoparticles with various volume fraction from 30% to 50%	57
Figure 26 Matching emissivity spectrum of PS thin layer doped with Au nanoparticles and absorption bands of Ethidium w/ DNA complex and Hemoglobin	59
Figure 27 Selective thermal emitter samples wit multilayer design (SiO ₂ - PS - Au)	60
Figure 28 Fabrication process of multilayer samples (SiO ₂ - PS - Au - Si)	61
Figure 29 Results from the experimental FTIR spectroscopy	64
Figure 30 Simulated hemispherical emissivity of a multilayer structure consisting of a SiO ₂ thin film on a PS thin film	65

LIST OF ABBREVIATIONS

CV	Cyclic voltammetry
DET	Direct electron transfer
DNA	Deoxyribonucleic acid
DPV	Differential pulse voltammetry
EIS	Electrochemical impedance spectroscopy
GCE	Glass carbon electrode
GE	Gold electrode
GOD	Glucose oxidase
H ₂ SO ₄	Sulfuric acid
HCl	Hydrogen chloride
IR	Infrared
IUPAC	International Union of Pure and Applied Chemistry
NaOH	Sodium hydroxide
NP	Nanoparticle
PANI	Polyaniline
PhC	Photonic Crystal
PS	Polystyrene
PV	Photovoltaic
STE	Selective thermal emitter
TE	Transverse electric
TiO ₂	Titanium dioxide

TM	Transverse magnetic
TONT	Titanium dioxide nanotubes
TPV	Thermo photovoltaic
UV	Ultraviolet

LIST OF SYMBOLS

c_0	Speed of light
d	Layer thickness
k	Wave vector
k_p	In-plane wave vector
n	Refractive index
N	Layer number
R	Fresnel reflection coefficient
\tilde{R}	Generalized reflection coefficient
f	volume fraction
x_m	Size parameter matrix material
x_{NP}	Size parameter nanoparticle
α	Absorptivity
$\alpha(r)$	Size dependent extension
ε	Dielectric function/permittivity
ε_b	Permittivity of bulk material
ε_m	Permittivity of host material
ϵ	Hemispherical emissivity
θ_1	Incident angle
θ_2	Refraction angle
λ	wavelength

ρ	Reflectivity
τ	Transmission
Υ	Damping constant
ω	Angular frequency
ω_{LO}	Longitudinal optical phonon frequency
ω_{p}	Plasma frequency
ω_{TO}	Transvers optical phonon frequency

CHAPTER 1 – INTRODUCTION

In the last decades, biosensors have become the most commonly used technique in medical detection applications. Biosensors combine the advantages of high selectivity and sensitivity with a high potential in low cost fabrication and miniaturization [1]. A considerable interest has been taken in new detection sensors, due to the fact that the percentage of human deaths caused by cancer is increasing and in addition the clinical detection techniques are time-consuming, expensive and still might lead to negative surgery results. Several label-based and label-free sensors have been introduced for lung and breast cancer cells [2,3,4,5].

The sensing properties of biosensors are defined either by their biological recognition element or the applied transducer, where the transducer is transforming the biological/chemical reaction into a signal, which then could be analyzed. The use of selective thermal emitters as transducers in order to analyze samples based on their radiation properties is a new promising technique. These emitters are commonly used as non-transmitting photonic crystals. Due to various geometrical structures or applied materials the emissivities of these crystals can be adjusted, as it is needed. [5] [6] [7]

In this study, a new transducer using nanoparticles instead of the biological recognition element is proposed. Therefore, a short insight in the fundamentals of biosensors, various transducer systems and their applications are given. In Addition, the basic functionality and designs of selective emitters are summarized with a focus on thermo photovoltaic systems and applications in this field.

Within the third chapter, the used tools are explained. This includes a detailed description of the assumed working principle. Based on the physical principles the calculation method in order to determine the hemispherical emissivity of selective thermal emitters is given. By means of this calculation, a MATLAB code is generated, which is used to simulated the emissivities of various designs of such emitters in the visible/near-ultraviolet (UV) region as well as in the infrared (IR) region. The analyzed designs are thin films of polar materials, polymers and polymers doped with gold (Au) nanoparticles of various volume fractions.

Subsequently, absorption spectra of biological molecules and chemical compounds are compared with the simulated designs. Moreover, selective thermal emitter samples are experimentally investigated and their emissivity spectra are compared with simulated results. Finally, a conclusion is drawn in order to summarize the study and provide an outlook to future work.

CHAPTER 2 – REVIEW OF LITERATURE

In the following chapter, a review of biosensors and selective thermal emitters is given. That includes the basic functional principle of biosensors, their classification based on the transducer and various applications of biosensors and their characteristics. Furthermore, the functionality of selective thermal emitters is explained with a focus on their application for thermo photovoltaic (TPV) systems.

2.1. Biosensors

In terms of the simplest definition, Biosensors base on the close spatial connection between a biological recognition element and the transducer, which is transforming the biochemical processes into a measurable signal (Figure 1).

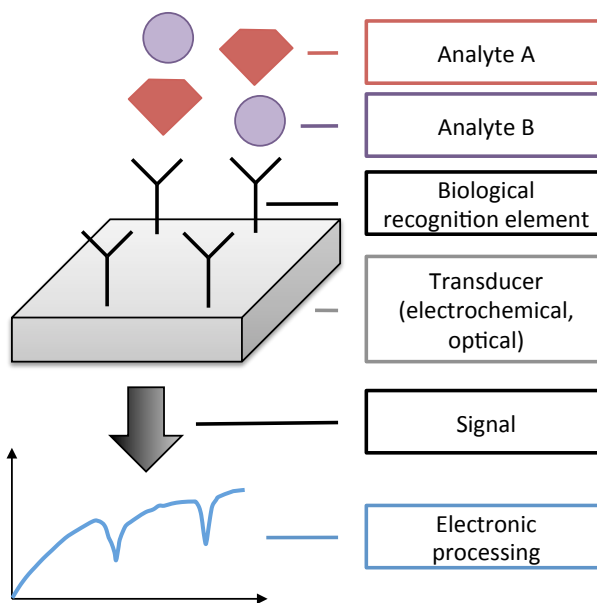


Figure 1 Basic structure of biosensors consisting of a biological recognition element and a transducer, which is generating a signal that can be analyzed after electronic processing

The binding reactions between the target analytes in a sample and the recognition element cause a signal, which could be electrical current or voltage among others. The transducer is then converting this signal into electrical data that can be analyzed and visualized by means of the right software [8]. Furthermore, the International Union of Pure and Applied Chemistry (IUPAC) defines a biosensor as a sensor with an integrated, sensitive biological component, which is either directly connected with the transducer or integrated into it. The usual objective is to generate a signal that is either proportional to the concentration of one specific analyte in the sample or to several analytes [9]. The biological elements, which have been used as a recognition element, vary widely over almost all known chemical categories including proteins (enzymes), nucleic acids (DNA), lipids, carbohydrates and combinations between these groups as well as living cells [10].

Biosensors are applied in several fields. In the field of environmental analysis they can be used to analyze the pollution of water in lakes and rivers as well as in the drinking water network. Moreover, biosensors are applied in process control and food analysis (e.g. to detect antibiotic residues) [11] [12] [13] [14] [15] [16]. Of importance are also applications in fundamental research in order to detect macromolecules and their interactions in biological media [17]. However, in the last 2 decades an increasing use of biosensors in the field of clinical diagnostics can be noticed [18] [19]. These already established measurement systems could be seen as precursors to today's biosensors and serve to control concentrations of glucose or lactate in blood and urine samples [18] [20] [21] [22]. Furthermore, DNA-tests, which serve to detect hereditary diseases and the resulting risks, are commonly used [23] [18] [24].

The selectivity and specificity is limited by the quality of the biological recognition element. Primarily the transducer determines the sensitivity of the sensor. Thus, biosensors can be classified by the biological recognition element as well as by the transducer [25]. However, this study focuses on developing a principle in order to detect analytes through their radiation properties. Therefore, biosensors are categorized in the following by their transducer and not by their recognition element.

2.2. Categorization of Biosensors

In the following section various fundamental transducer principles are explained in detail. That includes biosensors using electrochemical, optical and piezoelectric transducer. In addition, applications of these biosensors are introduced as well.

2.2.1. Optical transducer

Optical transducers take advantage of various optical phenomena: the surface Plasmon resonance on a sensors surface, Fluorescence [26] [27] [28], reflectometric interference spectroscopy [17] and Chemiluminescence [29] [30]. In the following, the surface Plasmon resonance and the Fluorescence are explained in more detail.

The surface Plasmon resonance bases on the interaction of incident light with free electrons of the metals surface. In the case of total reflection of the incident light generates a so-called evanescent field, which is characterized by a limited penetration depth. For resonance conditions, this field is able to interact with the thin metallic surface and generate surface Plasmon polaritons (SPP), which are coupled oscillations of free electrons and electromagnetic wave that propagate along the boundary between a polar material and a metal. These can be detected by surface Plasmon resonance

spectroscopy (SPRS) and are applied e.g. to detect protein- as well as DNA bindings [31] [32].

Fluorescence is a natural phenomenon that is characterized by spontaneous emission of light shortly after the sample has been excited. In the field of biosensing fluorescence marker are applied, in order to mark/react with the target analyte in solution. Due to the fact, that each combination of marker and analyte has its own unique emission wavelength, the target analyte can be detected by using fluorescence spectroscopy [31] [33] [34].

Applications of optical Biosensors

Biosensors base on fluorescence can be applied for medical diagnostics. Therefore, Oubaha et al. introduced a new multianalyte biosensor platform combing the characteristics of channel waveguides and fluorescent antibody detection. This sensor is fabricated by s sol-gel synthesis method, which is easily structurable by photolithography processes [35].

In order to fabricate their optical sensors, Oubaha et al. are using a fabrication process that could be roughly described by three key steps as shown in Figure 2. At first, the guiding wave channel is deposited on a substrate by photolithography. Therefore, the entire surface of initial substrate is covered with the guiding layer material by a spin-on process. Afterwards, this layer is exposed with UV light through a photomask. By means of the UV light the desired pattern is getting solid whereas etching can remove the rest of the layer.

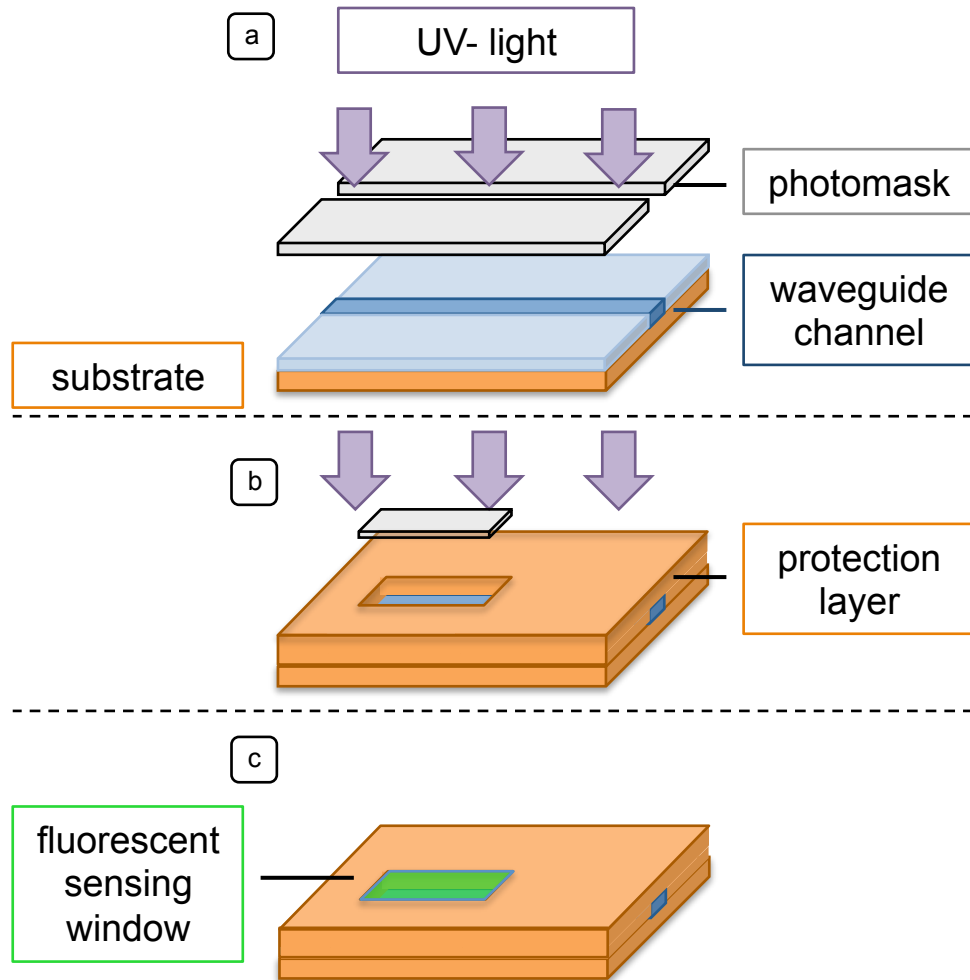


Figure 2 Optical waveguide sensor - fabrication steps [35]

In the second step, a protection layer is deposited on top, which covers the guiding wave channel. In order to generate sensing windows, which will be filled with the fluorescent antibody in the end, photolithography is used, as well. This needed sensing window results after etching the protective layer and deposition of the desired antibody. In order to determine the analyte concentration, the fluorescent antibody is excited by the wave, led through the guiding channel. A CCD camera then collects and quantifies the resulting fluorescence. The obtained fluorescence intensity can then be statistically be analyzed.

The setup Oubaha et al. [35] introduce, is able to detect biomolecules easily, with a limit of 0.25 µg/ml. Moreover, they proved that fluorescent antibody detection, where the sensing properties are enhanced by means of a guiding wave channel, are capable to be employed as biosensors. Additionally, they suggest several other functional groups, which could be applied for detection including functional nanoparticles, designed for specific immobilization.

2.2.2. Electrochemical transducer

Electrochemical transducers take advantage of redox reactions on the electrode surface, which can be quantified by measuring either the occurring current (amperometry) or potential difference (potentiometry) [36] [37] [38].

The amperometric method is suitable for metabolic products, which can be easily oxidized or reduced (e.g. Glucose, Cholesterol or lipid). Therefore, inside a measurement chamber, the current is recorded between two electrodes by constant voltage. The actual redox reaction is characterized by the current-voltage characteristic curve. Furthermore, the concentration of the analyte in the sample can be determined. The potentiometric method is suitable for ionic reaction products. The electric potential is the basis for the quantitative determination of these ions. It is recorded by the use of a measurement electrode, which is covered with a suitable recognition element in order to detect a certain analyte. The potentiometric method is commonly used for the detection of urea, creatinine or amino acids [10].

The control over the electrical parameter is the biggest advantage that is provided by the electrochemical transducer. Adjusting the electrode potential can control the selectivity over the analyte. Moreover the results are not depending on the geometry

and size of the electrodes what makes it possible to design biosensors in micro- to nanoscale dimensions [10].

Applications of electrochemical Biosensors

Zhu et al. [39] introduced a new composite in order to detect immobilized glucose oxidase (GOD). Therefore, they created a new composite consisting of polyaniline (PANI) coated titanium dioxide (TiO₂) nanotubes (TONT). The fabrication process and the reaction scheme of the introduced biosensor are shown in Figure 3.

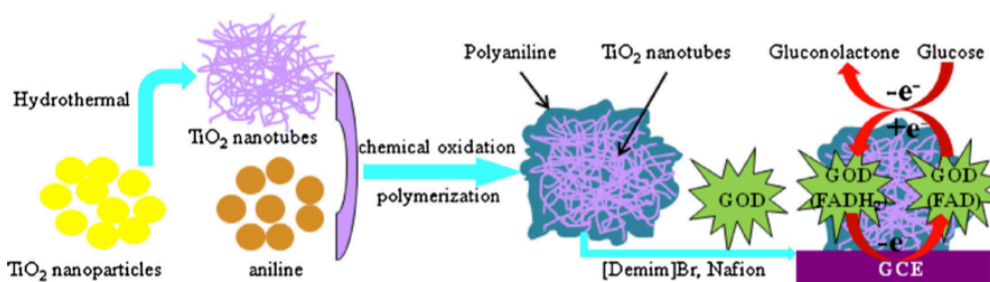


Figure 3 The Fabrication of TiO₂ nanotubes and the measurement process to detect glucose [39]

In order to synthesize this composite, Zhu et al. firstly transform TiO₂ nanoparticles (NP) into TNTs by using hydrothermal reaction. This method includes the following steps: at first the TiO₂ NPs are added into sodium hydroxide (NaOH) aqueous solution before the actual reaction starts in an autoclave. After this reaction the product is washed with hydrochloric acid (HCl) and then adjusted to pH 7.0 by adding distilled water. This process is repeated three times. In the last step the solution is centrifuged and dried in oven at 60°C. The resulting nanotubes are then coated by polymerizing aniline using chemical oxidation polymerization method [39].

In order to use the synthesized PANI-TONTs as an electro-catalyst, brominated 1-decyl-3-methyl imidazole ([Demim]Br) and Nafion are added and the mixture is

deposited onto a glass carbon electrode (GCE). By adding the GOD onto this GCE the redox reaction gets started. By applying cyclic voltammetry, the now existing redox current can be measured and occurring change can be used to detect immobilized glucose oxidase.

Zhu et al. show that an electrochemical biosensor of TiO₂ nanotubes coated by polyaniline can be used to detect Glucose. Moreover, they point out, that coating the nanotube leads to a ~55% higher direct electron transfer (DET), which they reduce to the better electrical conductivity of PANI [39].

In their paper Benvidi et al. introduce a new electrochemical biosensor in order to detect breast cancer, in particular breast cancer in its initial stages (BRCA1). Breast cancer is the most commonly diagnosed cancer, which is responsible for lots of death among women. Usually the clinical techniques for the determination of breast cancer are time-consuming. In order to enhance the detection of BRCA1 the authors present a biosensor based on a label-free electrochemical impedance method, which is characterized by a high sensitivity and reproducibility [2].

Similar to Zhu et al. [39], Benvidi et al. [2] also use an Au electrode (GE) in order to create an electrochemical biosensor. Among other commonly used metals, like Platinum (Pt), Silver (Ag) and also Carbon (C), Au is the mostly frequently used metal. Under ambient conditions, it does not form a stable oxide and thus, it works as a perfect catalyst for redox reactions.

Figure 4 presents the 4 process steps, which are necessary in order to immobilize/synthesize the target DNA onto the Au electrode (GE).

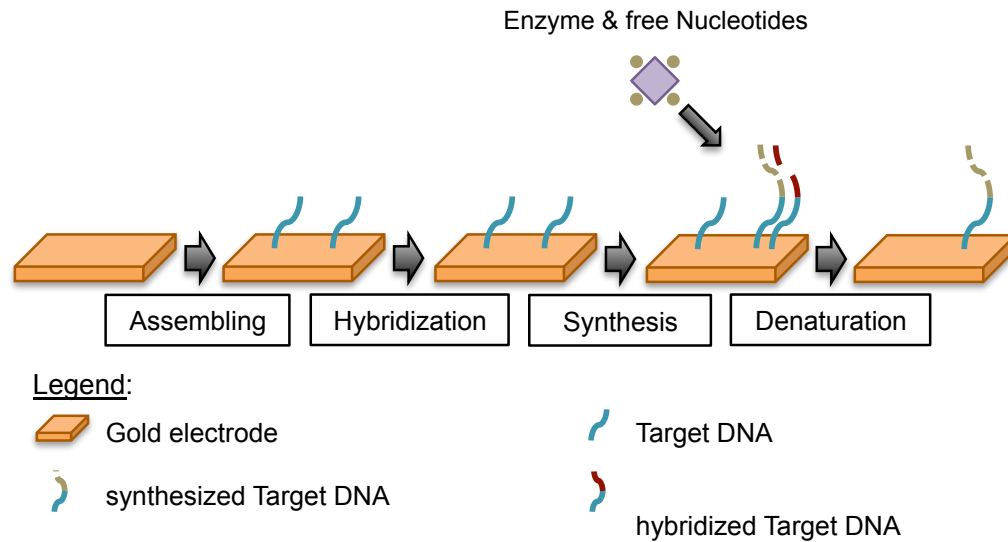


Figure 4 The process steps in order to immobilize/synthesize the target DNA onto the Au electrode (GE) [2]

At first, they placed the ssDNA (Target DNA), which is a segment of the breast cancer (BRCA1), onto the GE. Therefore, the electrode is electrochemical cleaned with sulfuric acid (H_2SO_4) and washed with ethanol. Then a solution (including the DNA sample) is placed on the electrodes surface in a wet chamber before it is kept at room temperature for the immobilization process. For the hybridization, a buffer solution containing a certain concentration of the complementary target ssDNA is placed on the electrode. After the hybridization, the electrode is washed again to remove all the unhybridized ssDNA.

Adding the tag enzyme into the DNA synthesis environment leads to an increasing DNA probe length. The growth of the DNA probe significantly enhances the charge-transfer resistance, which increases the selectivity and sensitivity of the biosensor. In the last step (denaturation) the target DNAs are eliminated and just the synthesized probes remain at the electrode.

During all of these steps Benvidi et al. measure the changes by using electrochemical impedance spectroscopy (EIS), cyclic voltammetry (CV) and differential pulse voltammetry (DPV). In particular, EIS is a commonly used label-free measurement technique for molecular reactions at electrode surfaces. EIS transduces changes in interfacial properties between the applied electrolyte, which produced by DNA hybridization process and the working electrode. One of the biggest advantages of EIS method is, that no label (e.g. fluorophore) is needed to mark the target DNA. Moreover, electrochemical biosensors base on EIS provide high sensitivity and selectivity by lower cost and the ability to work in micro- and nanoscale application.

Benvidi et al. [2] show that under laboratory conditions the detection by using EIS method provide a better sensitivity for lower concentration of the target DNA as the DPV. With this higher selectivity and sensitivity the designed label-free biosensor could successfully determine breast cancer.

2.2.3. Piezoelectric biosensors

Piezoelectric biosensors use acoustic waves in order to detect molecule bindings on a surface in real time. Therefore, they either measure the propagation of such waves throughout or along the surface of a piezoelectric substrate. The propagation of these waves along a surface is influenced by contamination, absorption caused by analytes and the optical properties of the surrounding medium.

As a signal the displacement of resonance frequency or the change in the propagation speed of the wave are used. In order to monitor immunological interactions piezoelectric sensors based on the quartz crystals microbalance are applied commonly [40] [41].

2.3. Selective thermal emitters and their application

2.3.1. Selective thermal emitters

Selective thermal emitters are nano- or micro-scale structures, which provide a unique spectrum of emissivity depending on different materials and their modification. They can be applied to create new or modify existing emissivity spectra for several applications. These could be enhancing the efficiency in energy conversion systems as well as detecting bio- or biochemical molecules in sensor systems [44].

Commonly, selective thermal emitters are generated by Photonic Crystals (PhC). According to the definition, PhCs have a periodic structure made of materials with different refractive indices (n), which is defined by the material depending dielectric constants permittivity ϵ and permeability μ [45] [32]. Sajeev John and Eli Yablonivitch, who published their theoretical theory independently of one another in 1987, firstly introduced the concept of PhC [46] [47]. It is based on the idea of creating a artificial material that shows similar phenomenon's of photons like electrons do in semiconductors

Photonic Crystals are structures with a spatial periodic change of the refractive index. They can be classified based on their dimensions. Therefore, a distinction is made between one-dimensional (1D), two-dimensional (2D) and three-dimensional (3D) crystals according to the number of spatial directions, in which the refractive index is changing. (Figure 5) The refractive index is always positive. This index can be complex for absorbing materials [6] [32]. A periodic series of layers of materials with different refractive indices is the easiest way of a one-dimensional Photonic Crystal (a). 2D crystals are characterized by a refractive index, which changes into two

different spatial directions. Following this rule, in a 3D PhC the refractive index is changing in 3 different dimensions (c).

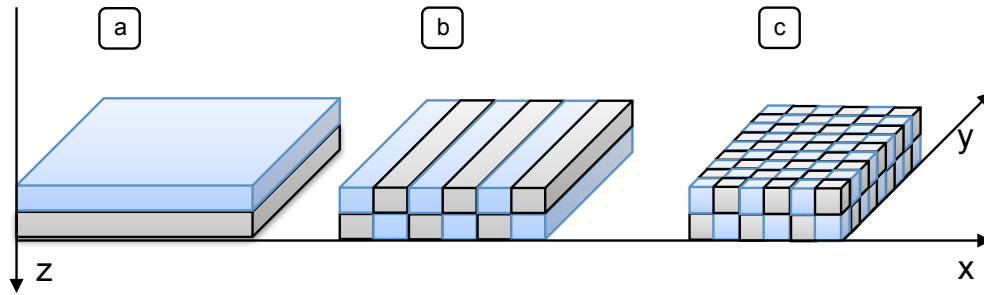


Figure 5 Various Photonic Crystal Designs, a) 1D, b) 2D, c) 3D

2.3.2. Application in energy conversion systems (TPV)

The simplest way to apply selective thermal emitters in energy conversion systems is to enhance the efficiency of thermo photovoltaic (TPV). TPV systems use the thermal radiation emitted from hot bodies to transform this thermal energy into electrical energy. Therefore, these systems use the same principle as known from photovoltaic (PV) cells. Such TPV cells usually consist of a radiative heat source; an emitter, filter and a conventional PV cell as shown in Figure 6 [48].

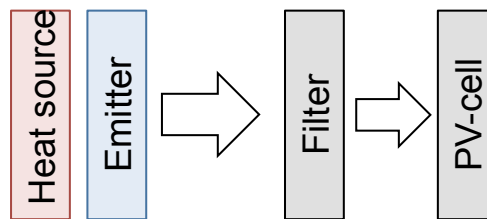


Figure 6 Functional structure of conventional TPV systems without selective thermal emitter [48]

In order to enhance the efficiency of conventional TPV systems different designs and materials are used for selective thermal emitters. According to Ye et al. increases

the application of a vanadium dioxide (VO_2) two dimensional selective emitter the system efficiency by about 50% than with an silicon carbide (SiC) emitter. The applied selective emitter consists of a periodic layer of cylindrical micro cavities, filled with air as shown in Figure 7. Due to the geometrical structure of the VO_2 layer forming the micro cavities, the spectral emissivity is depending on the parameters cavities depth and radius. Moreover, Ye et al. point out that the range, where the emitter emits its radiation is increasing with higher radii. At the same time, increasing depth for smaller wavelength leads to higher emissivities [49].

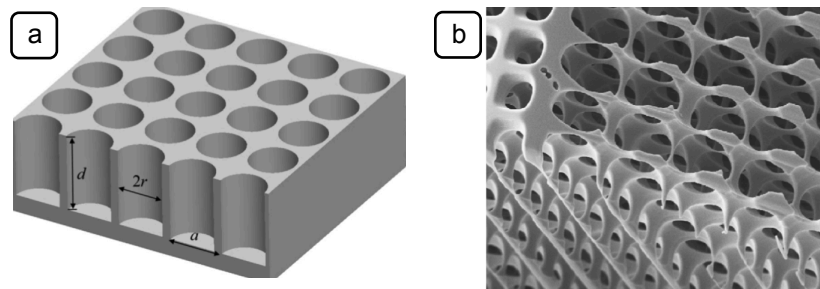


Figure 7 Examples of 2D [49] and 3D [50] photonic crystal designs

Another way to increase the efficiency of TPV systems is to use a 3D photonic crystal instead of a 2D design. A 3D design can be realized by coated macroporous structures. Therefore, Garín et al. introduce a silicon (Si) scaffold which is coated with Pt. Due to electrochemical etching process the surface oxidases, which, in particular, leads to a Si/SiO₂/Pt structure. This metal-dielectric structure is characterized by a good thermal structure due to the Si scaffold with optical properties defined by the metal coating. However, Garín et al. observed a sharp emissivity increase at $\lambda = 3 \mu\text{m}$ [50].

CHAPTER 3 – METHODOLOGY

In the following section, the basic functionalities of biosensors and selective thermal emitters are merged in order to suggest a sensing device using the emissivity in order to detect analytes. Therefore, its basic principle is explained theoretically in the first step. Afterwards the applied calculation model is explained, including the necessary, physical fundamentals are presented, as well. This calculation is implemented in MATLAB in order to solve them analytically and simulate various structures. Comparing the results with the results already published validates the correctness of the self-written code.

3.1. Basic functionality

All matter is emitting radiation continuously. This so-called thermal radiation bases on thermal vibration of the particles of the matter like electrons, photons or atoms. Due to the unique behavior of each molecule, the emitted radiation can be interpreted as a fingerprint. In order to compare the radiation behavior of different real bodies, the hemispherical emissivity is commonly used.

Based on this unique fingerprint of each molecule a new way of detecting molecules in biological samples (e.g. DNA or cells in solution) is proposed in this study. This detecting process can be divided into two principles, which are combined in the end.

The first theoretical principle could prove, how analyzing the hemispherical spectrum could lead to the detection of molecules in a sample. Therefore, in a first step a selective thermal emitter is designed and its emissivity spectrum is obtained by analytical calculation and experimental measurement methods. After this a droplet of the investigated solution is deposited on top of the selective thermal emitter. Due to this new layer the spectrum changes and by analyzing this change the molecule of interest could be detected. The Figure 8 shows the principle clearly.

On the left side of the figure a photonic crystal, which is used as the detector, and its unique spectrum of emissivity are shown. The crystal consists of a thin film (layer thickness in the scale of microns) of a polar material (e.g. SiC) deposited on a substrate coated with a high reflective material (e.g. Au). The substrate is necessary in order to make this setup workable.

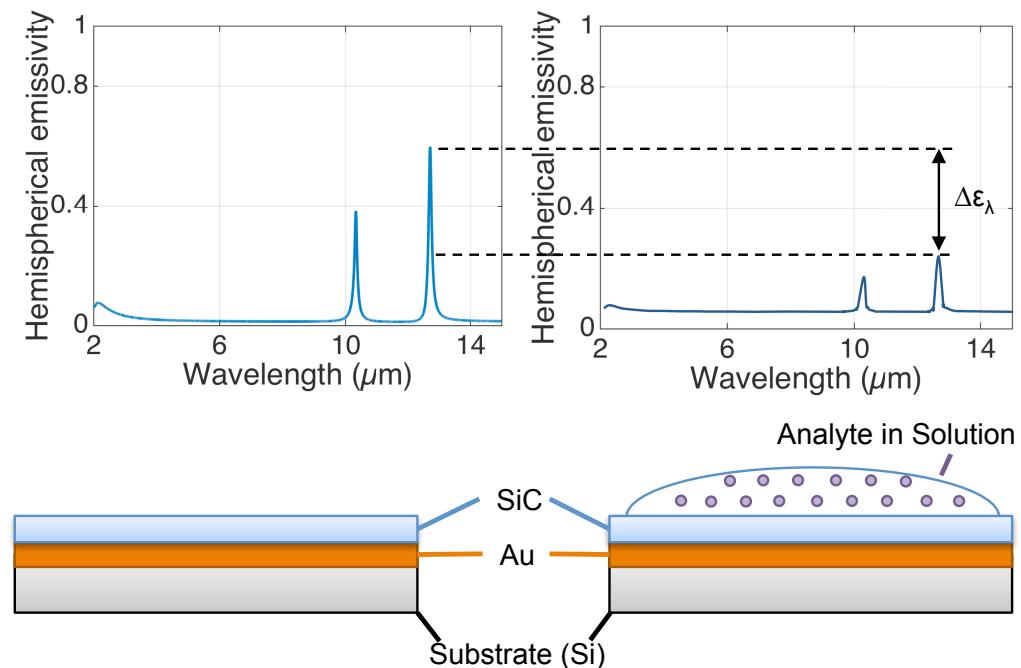


Figure 8 Basic principle of how a sample droplet on top of a selective thermal emitter influences the hemispherical emissivity.

The spectrum of emissivity of such a photonic crystal can be theoretically calculated by using the specific optical properties of polar materials and the formula for the reflection coefficient. This analytical calculation method is explained in detail in section 3.2. The right side of the Figure 8 shows the setup, how molecules in a sample could be detected in the range of near-field infrared radiation. The droplet on top of the emitter forms a new layer, which influences the hemispherical emissivity of the setup. If the spectrum of emissivity of the designed selective emitter is matching the unique spectrum of the molecule of interest, it is assumed that the additional layer, created by the sample droplet, changes the resulting emissivity spectrum of the setup. The difference in the spectrum at the wavelength of change indicates the molecule of interest in the sample, due to its own unique spectrum of absorption.

The second assumed principle is applied to quantify the sample regarding the amount of molecules. Therefore, a selective thermal emitter with a metal-doped layer of polymer is designed and the theoretical, hemispherical emissivity is calculated in a first step. Again, the sample is deposited as a droplet on top of the emitter and after a heating process, it is assumed that the molecules diffuse into the layer and react with Au nanoparticles. This reaction is increasing the volume fraction of nanoparticles in polystyrene (PS). Figure 9 shows this functional principle clearly.

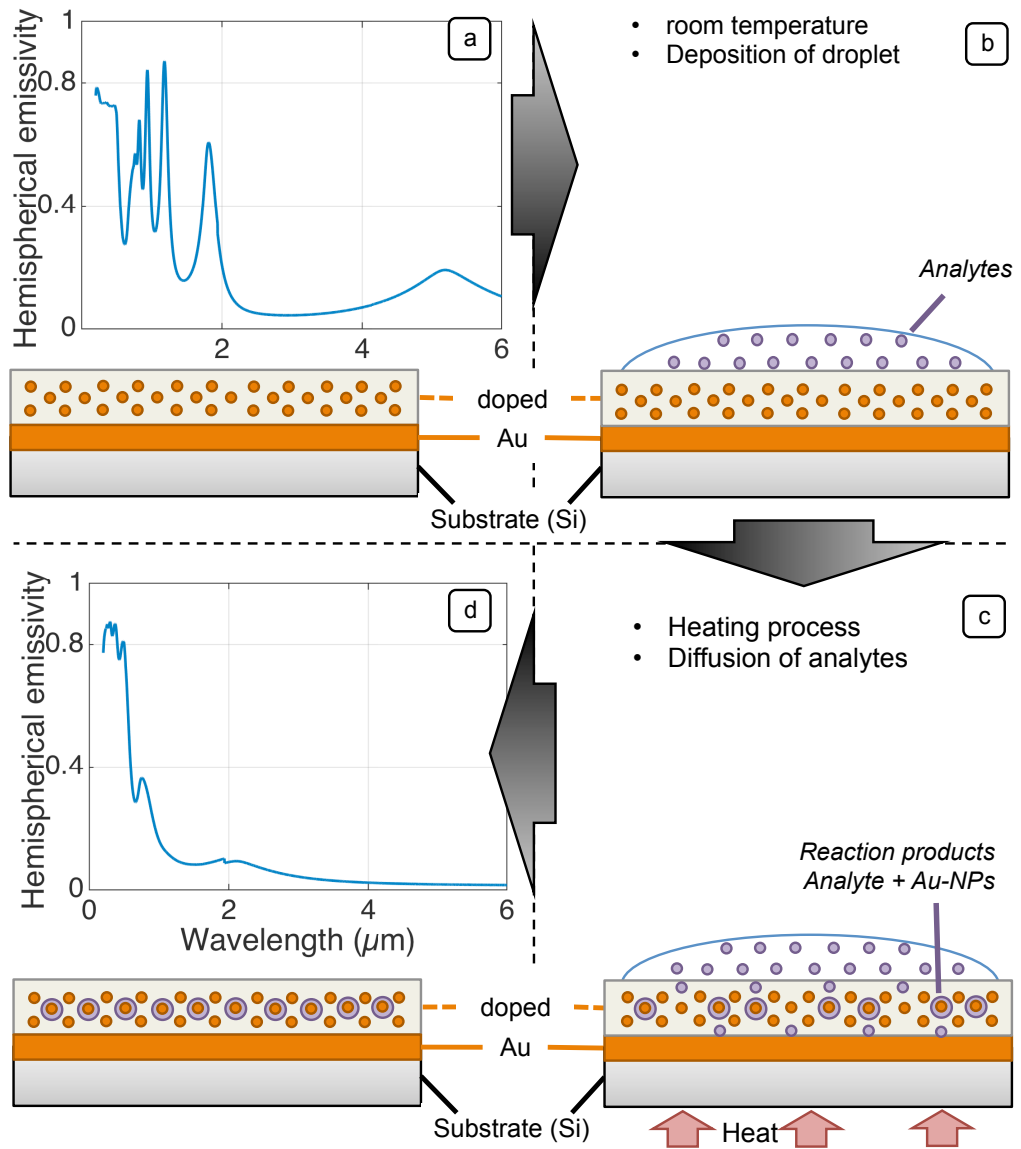


Figure 9 The basic principle in order to quantify the sample in the visible/near-UV spectrum

In the first step (a), the photonic crystal, which is applied to quantify the sample, is shown with its unique spectrum of emissivity. The structure of this detector crystal is similar to the one explained before. However, instead of the thin film of polar material a layer of metal-doped polymer is deposited on a substrate coated with a high reflective material (e.g. Au). The spectrum of emissivity of such a structure can be

theoretically calculated by using the effective dielectric function (see section 3.2.3) and also the formula for the reflection coefficient as explained in section 3.2.4.

The top right side of the Figure 9 (b) shows the setup after the solution, including the molecule of interest, has been deposited on the emitter at room temperature. In order to measure the hemispherical emissivity of the prepared sample, it is heated up to a temperature, which is high enough to soften the polymer layer and support a chemical reaction, but is also low enough to not melt the polymer or destroy the molecules of interest (e.g. by denaturation) (c). After a certain time of heating it is assumed that all the molecules have been diffused into the layer and (partly) reacted with the NPs. It is assumed that, the reaction products have different optical properties than the pure NPs, thus the actual concentration of NPs is reduced and the spectrum of emissivity is assumed to be comparable to one of less volume fraction. In the end (d), the solution rest is cleaned from the crystal and the emissivity of the modified PS-layer could be measured.

3.1.1. Design boundaries and constraints

Materials and their characteristics

The selective thermal emitters, which are investigated in this study, are either one or two (multilayer) thin films of a material on a substrate coated with a high reflective metal. Here, Au is used for all designs to be the reflective material. Moreover, three different material groups, which could form the thin film layer, are investigated. These materials are commonly used materials for selective thermal emitters as well as for biosensors. In Figure 10, the groups polar materials (e.g. SiC, BN) including

combinations of both to create doped materials (a), pure polymer (e.g. PS) (b) and polymers doped with nanoparticles (PS+NPs) (c) are shown.

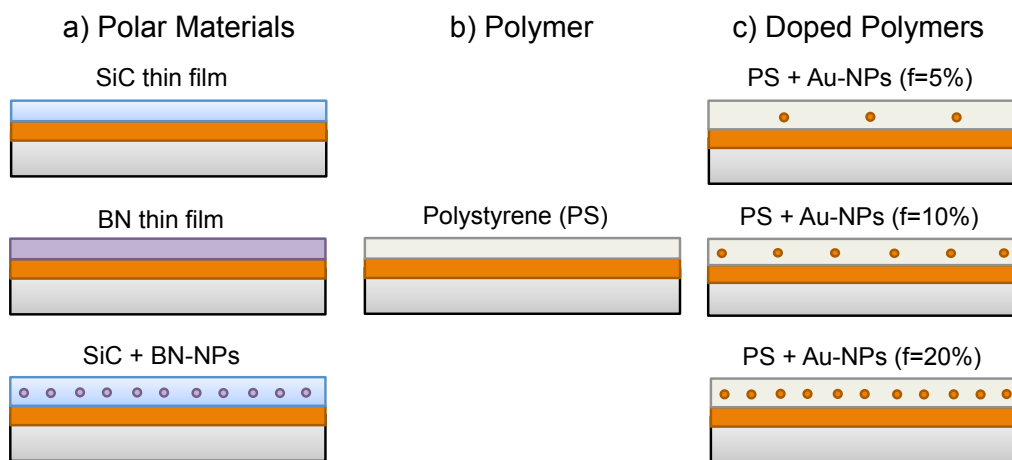


Figure 10 Material groups of interest in this study: polar materials, polymers, doped polymer

The polar materials SiC and boron nitride (BN) are typical materials for STEs. Both of them show a high absorbance signature in the IR range of the spectrum. This spectral range is of major interests for the detection of chemical molecules (TNT) [51]. Moreover, both materials can be combined to form doped materials. Therefore, either BN nanoparticles are added to a SiC matrix or vice versa. The second group is pure polymer. In the framework of this study it used as a reference for the group of doped materials.

In this study the group of doped materials is formed by the combination of PS as the matrix material and Au nanoparticles. By varying the volume fractions of Au NPs from 5% up to 50% by using a step width of 5% different properties and emissivity spectra can be reported. Furthermore, other materials could be used as nanoparticles like copper (Cu) and Ag. Due to its ability to not form stable oxides under ambient

conditions, Au can easily be paired with several biomaterials, such as DNA [52] [53], by either working as a working electrode for electrochemical sensors or working as binding reagents for molecules in solution for optical sensors [2] [3] [53] [54].

Calculation constraints

In this study, the hemispherical emissivity is considered to be analyzed and thus serving as a benchmark. Therefore, for all simulations and analysis the following assumptions are made: the incident waves are monochromatic plane waves, the materials are opaque, homogenous and isotropic, and all the surfaces and interfaces of emitters are optical smooth,

In the following section the calculations for irradiating electromagnetic waves at an interface between two different medias are conducted for the assumptions that these waves are monochromatic plane waves [44] [55] [56]. Monochromatic plane waves are defined by having the wavefront perpendicular to the wave vector k . Additionally, the phase is constant and given by $kx - \omega t = const$. In that case, the absolute value of the wave vector ($k = |k|$) is also called *wavenumber*.

Furthermore, the reported results of this study base on the assuming the applied selective thermal emitters to be opaque. Opaque materials are defined as materials, which do not allow the transmission of radiation ($\tau = 0$). In order to guarantee this characteristic, the substrate is coated with a thin layer of a high reflective material (Au). This coating works as mirror and is assumed to reflect 100% of the irradiating radiation. Thus, the used selective thermal emitters can be defined to be opaque.

For these materials Kichhoff's law can be applied. It states that the absorption of a medium is equal to its emittance ($\alpha = \epsilon$), thus the radiation properties of an

opaque body can be completely described by the reflectance (ρ) and emittance (ϵ). Considering the law of nature that all radiations have to be reflected, transmitted or absorbed and also applying Kirchoff's Law, the emittance can be completely described by the reflectance:

$$\epsilon = 1 - \rho \quad (1)$$

Additionally, the materials are not just assumed to be opaque but also homogenous. For electromagnetic waves of certain wavelengths thermal selective emitters can form photonic band gaps, which is comparable to the electronic band gap of semiconductors. Thus, it is impossible for these waves to propagate within the crystal. Furthermore, if the wavelength λ is much less than the lattice constant of the material the refraction follows the laws of geometric optics. Thus, the incident wave gets scattered just at interfaces between two media, due to the changes in the refractive indices [45] [57] [58].

Furthermore, the surface of each layer and interface is assumed to be optical smooth. A rough surface could be caused by two different ways: Due to the fabrication process and also due to intended surface grating, which are both neglected in this study.

3.2. Calculation of hemispherical emissivity

The emissivity (ϵ) correlates the radiation characteristics of real bodies with the ideal radiation characteristics of black bodies at the same temperature over all

wavelengths. That leads to the analytical definition as a ratio of real body emittance to black body emittance.

$$\epsilon = \frac{\textit{realbody emittance}}{\textit{blackbody emittance}} \quad (2)$$

A body is called to be a black body if it is neither reflecting nor transmitting radiation. This theory describes the ideal radiation behavior. Furthermore, a black body absorbs the entire specific irradiation which leads, in consideration to Kirchhoff's Law, to $\alpha = \epsilon = 1$ with $\tau = \rho = 0$, where α is the absorbance, τ is the transmission and ρ is the reflection, defined by:

$$\rho = \frac{\textit{reflected flux}}{\textit{incident flux}} \quad (3)$$

$$\alpha = \frac{\textit{absorbed flux}}{\textit{incident flux}} \quad (4)$$

$$\tau = \frac{\textit{absorbed flux}}{\textit{incident flux}} \quad (5)$$

Following Kirchhoff's Law, black bodies emit the maximal possible energy at each temperature, thus they also have the maximal possible emittance. The consequence of this is that the emissivity of black bodies is equal to 1 and due to the fact that real bodies are not perfect absorbers ($\alpha < 1$) their emissivity equals to values between 0 and 1. There are no black bodies in reality, however the sun is pretty close to one [59].

However, analytically the hemispherical emissivity of a real body equals to the integral of the spectral hemispherical emissivity over the entire half-space: [59]

$$\epsilon_\lambda = \frac{\lambda}{4\pi^2} \int_0^{2\pi/\lambda} k_\rho \sum_{t=TE, TM} \left(1 - |R_{1,2}^{(t)}|^2\right) dk_\rho \quad (6)$$

Here, k_ρ represents the in-plane wave vector k and $\sum_{t=TE, TM} (1 - |R_{1,2}^{(t)}|^2)$ represents the spectral hemispherical emissivity for both the transverse electric (TE) and transverse magnetic (TM) polarized parts of an incident wave. Both key parts of the equation are explained below.

3.2.1. The wave vector k

Monochromatic waves oscillate with an angular frequency of ω . Thus, One oscillation would take them a time equal to $2\pi/\omega$, by definition. Assuming monochromatic waves are plane waves, the wavefront is then perpendicular to the wave vector k and the phase is constant and given by: $kx - \omega t = \text{const}$. Therefore, the absolute value of the wave vector ($k = |k|$) is also called *wavenumber*. Basically, this is a spatial angular frequency. The distance between two different wave fronts of one plane wave in the same phase is also known as wavelength and given as: [56] [60]

$$\lambda = \frac{2\pi}{|k|} \quad (7)$$

Assuming a vacuum as the media of propagation the wave vector can be determined by using the given formula for a constant phase:

$$k_0 = \frac{\omega}{c_0} \quad (8)$$

In this case c_0 is not just the speed of light in vacuum, defined as $2.998 \cdot 10^8$ m/s, but also the speed of propagation of the electromagnetic wave.

In this study the interface between the media is set as a x-y-plane, thus the in-plane wave vector k_i of the irradiation is perpendicular to this plane and is set to propagate in the x-z-plane as shown in Figure 11. Therefore, the y-component of the vector equals to 0 ($k_y = 0$). Due to a not existing y-component, the in-plane wave vector k_ρ is equal to the x-component and therefore, it can also be expressed as: $k_\rho = k_x$. By means of the geometrical relationship between the components of k the z-component is determined by the Pythagoras' theorem:

$$k_{z1} = \sqrt{k_1^2 - k_{x1}^2} \quad (9)$$

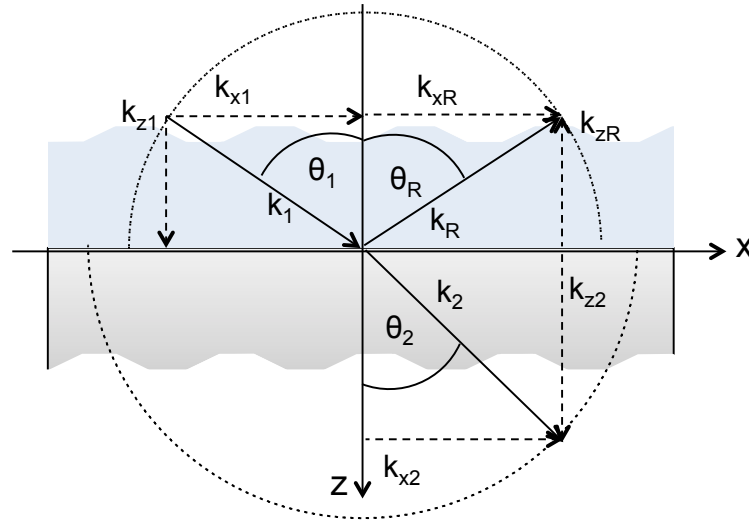


Figure 11 Interaction of the in-plane wave vector k_i at an interface between two media/layer [56]

Assuming a transition from an optical thinner into an optically thicker medium, electromagnetic waves incident under the angle of θ_1 , thus the refracted waves in medium 2 propagate under

$$\frac{\sin\theta_1}{\sin\theta_2} = \frac{n_2}{n_1} \quad (10)$$

The refraction at the interface also leads to a change in wavelength as well as in speed of propagation. In order to determine these changes, the refractive index n is applied. This index describes how the speed of propagation of a wave changes (increasing or decreasing) at an interface between two different media, e.g. vacuum and bulk material [55] [62]. Due to the fact that the angular frequency ω is constant [55], the specific wavelength in the material can be determined by means of the refractive index, as well:

$$n = \frac{c_0}{c_m} \quad (11)$$

$$n = \frac{\lambda_0}{\lambda_m} \quad (12)$$

The refractive index can also be written with the terms of permittivity and permeability [63]:

$$n = \sqrt{\frac{\mu_m \varepsilon_m}{\mu_0 \varepsilon_0}} = \sqrt{\mu \varepsilon} \quad (13)$$

By the means of the refractive index, the refracted wave vector propagating in media is determined by:

$$k^2 = \frac{\omega^2}{c_m^2} \varepsilon_m \mu_m \quad (14)$$

3.2.2. Complex refractive index

In the forgoing section the media is assumed to be non-absorbing, which leads to the permittivity and permeability to be scalar. In the further study polar materials (SiC and BN) will be applied for different structures of selective thermal emitters. These materials do absorb and therefore, the complex permittivity has to be applied to

describe the refraction processes at an interface completely. The complex permittivity is a function of the wavelength ($\epsilon(\lambda)$) [64]. This so-called complex dielectric function is defined as shown in equation (12). Due to the fact that polar materials are non-magnetic, the permeability of a medium μ_m can be assumed to be 1. Thus, the refractive index is just depending on the dielectric function and in the case of a complex function this is complex as well [63] [64]:

$$\epsilon = (n + ik)^2 \quad (15)$$

Where, $(n + ik)$ is the complex refractive index, n is the non-complex refractive index and k is the extinction coefficient. Usually both of them are called optical *constant* of a material even though neither the refractive index nor the extinction coefficient are constant over a wide spectrum [63].

3.2.3. Permittivity

Unfortunately, there is no general valid way to determine the permittivity (dielectric function) for all materials. Due to the fact that this study considers the material groups of polar materials, polymers and polymers doped with Au nanoparticles their specific equations to calculate the dielectric function are explained in the following.

The permittivity for **polar materials**, is given by [44] [65]:

$$\epsilon(\omega) = \epsilon_\infty \frac{\omega^2 - \omega_{LO}^2 - i\omega\gamma}{\omega^2 - \omega_{TO}^2 - i\omega\gamma} \quad (16)$$

It is depended on the angular frequency ω and some may call this equation the *polaritonic equation* [66] where, ϵ_∞ is the high frequency dielectric constant, γ is the damping constant and ω_{LO} and ω_{TO} are the longitudinal and transverse optical phonon

frequencies. These parameters are constant and the assumed values and dimensions for SiC and BN are given in Table 1 [65].

Table 1 Needed parameters to calculate the permittivity of polar materials SiC and BN [64]

	ω_{LO} [eV]	ω_{TO} [eV]	Υ [eV]	ϵ_{∞}
SiC	0.12	0.098	5.88×10^{-4}	6.7
BN	0.1616	0.1309	6.55×10^{-4}	4.46

The permittivity for **Polystyrene** is taken from [67] and approximated by the four-term-fit model shown in equation (17). The parameters and their dimensions are given in

Table 2 [67].

$$\epsilon(\omega) = 1 + \sum_{i=1}^{i=4} \frac{f_i}{(\omega_i^2 - \omega^2 - i\omega g_i)} \quad (17)$$

Table 2 Needed parameters to calculate the permittivity of PS [66]

ω_i [eV]	f_i [eV]	g_i [eV]
6.35	14.6	0.65
14.0	96.9	5.0
11.0	44.4	3.5
20.1	136.9	11.5

In order to determine the permittivity of **doped materials** the theory of the effective media theory has to be applied. For a composite material consisting of a

matrix containing nanoparticles the effective permittivity is given by the Clausius-Mossotti equation: [68] [69]

$$\varepsilon_{eff}(\omega) = \varepsilon_m \left(\frac{r^3 + 2\alpha(r)f}{r^3 - 2\alpha(r)f} \right) \quad (18)$$

Here, ε_m , r and f are the dielectric function of the matrix, the radius and volume fraction of nanoparticles, respectively. $\alpha(r)$ is the size dependent extension of the Maxwell Garnett formula, which can be determined by deriving using Mie theory, in particular the first electric Mie coefficient:

$$a(r) = \frac{3ic^3}{2\omega^3 \varepsilon_m^{\frac{3}{2}}} a_1(r) \quad (19)$$

$$a_1(r) = \frac{\sqrt{\varepsilon_{NP}} \psi_1(x_{NP}) \psi_1'(x_m) - \sqrt{\varepsilon_m} \psi_1(x_m) \psi_1'(x_{NP})}{\sqrt{\varepsilon_{NP}} \psi_1(x_{NP}) \xi_1'(x_m) - \sqrt{\varepsilon_m} \xi_1(x_m) \psi_1'(x_{NP})} \quad (20)$$

To solve the first Mi coefficient the dielectric function of the matrix ε_m and nanoparticles ε_{NP} as well as the Riccati-Bessel functions of the first order ψ_1 and ξ_1 of the size parameters of the matrix x_m and NPs x_{NP} are needed. The first order spherical Bessel function j_1 and the first order spherical Hankel functions $h_1^{(1)}$ are used to determine the Riccati-Bessel function of first order [68].

The permittivity for the matrix material can be determined by either the already explained polaritonic Eq. 16 or four-term-fit model Eq 17, depending on the chosen material group.

Due to the fact that metallic nanoparticles have shown to be size-dependent, their dielectric function is not only depending on the angular frequency but also on the radius of the NPs. Thus, the electron scattering effect has to be taken into account.

$$\varepsilon(\omega, r) = \varepsilon_b(\omega) + \frac{\omega_p^2}{\omega^2 + i\omega\Upsilon} - \frac{\omega_p^2}{\omega^2 + i\omega(\Upsilon + \frac{Av_f}{r})} \quad (21)$$

Here, $\varepsilon_b(\omega)$ is the dielectric function of the bulk material; ω_p is the plasma frequency; Υ is the damping constant; A is the proportionality constant and v_f is the Fermi velocity. The proportionality constant is depending on the electron scattering process at the NPs surfaces and is assumed to be unity.

The permittivity of the bulk material can either be determined by the already introduced equations for polar materials or PS. However the nanoparticles employed in this study are made of Au, thus the function for metals has to be applied. This is based on the free electron theory introduced by Paul Drude and given by [70]:

$$\varepsilon(\omega) = 1 - \frac{\omega_p^2}{\omega^2 + i\omega \frac{1}{\tau}} \quad (22)$$

According to Johnson and Christy [70], the Drude model is not valid for visible and near-ultraviolet (near-UV) regions (0.64-6.5 eV or 0.1879-1.9373 μm) due to not separating the free-electron effect from the interband transitions. Therefore, the values obtained by solving Eq. 22 are higher than the one Johnson and Christy were able to measure. In order to determine the dielectric function for Au NPs in this study, these measurements are used for the visible and near-UV range and for the infrared region the Drude theory is applied. According to Johnson and Christy this method is also valid for other metals, such as Ag and Cu.

3.2.4. Spectral hemispherical emissivity and refraction coefficient

Assuming the used photonic crystal to be opaque (no transmission), the spectral hemispherical emissivity (depending on the incident angle) can be derived from the rule that all radiation have to be either reflected or absorbed by matter:

$$1 = \alpha(\theta_i) + \rho(\theta_i) \quad (23)$$

By considering Kirchoff's Law ($\alpha = \epsilon = 1$) and transposing Eq. 23 as well as by the means of the Fresnel reflection coefficients $R_{1,2}^{(t)}$ with $t = TE, TM$, the spectral hemispherical emissivity can be derived by:

$$\epsilon_\lambda(\theta_i) = \alpha_\lambda(\theta_i) = 1 - \rho_\lambda(\theta_i) \quad (24)$$

$$\epsilon_\lambda(\theta_i) = 1 - \left| R_{1,2}^{(t)} \right|^2 \quad (25)$$

Therefore, the Fresnel reflection coefficients for a certain wavelength are calculated by the following equation considering if the wave is either transverse electric (TE) or transverse magnetic (TM) polarized [71].

$$R_{1,2}^{TE} = \frac{\mu_2 k_{z1} - \mu_1 k_{z2}}{\mu_2 k_{z1} + \mu_1 k_{z2}} \quad (26)$$

$$R_{1,2}^{TM} = \frac{\epsilon_2 k_{z1} - \epsilon_1 k_{z2}}{\epsilon_2 k_{z1} + \epsilon_1 k_{z2}} \quad (27)$$

Here, k_{z1} and k_{z2} are the z-components of the wave vector for media 1 and media 2, respectively. μ_1 and μ_2 as well as ϵ_1 and ϵ_2 are the permeability and permittivity of media 1 and media 2, respectively.

By using the Fresnel reflection coefficients the spectral hemispherical emissivity $\epsilon_\lambda(\theta_i)$ can easily be determined for a system consisting of 2 different media. However, for further investigations systems consisting of more than 2 layers are

considered. Therefore, these coefficients have to be extended. Thus, the generalized reflective index $\tilde{R}_{n,n+1}^{(t)}$ with $t = TE, TM$ is introduced:

$$\tilde{R}_{i,i+1}^{(t)} = \frac{R_{i,i+1}^{(t)} + \tilde{R}_{i+1,i+2}^{(t)} e^{i2k_{zi+1}(d_{i+1}-d_i)}}{1 + R_{i,i+1}^{(t)} \tilde{R}_{i+1,i+2}^{(t)} e^{i2k_{zi+1}(d_{i+1}-d_i)}} \quad (28)$$

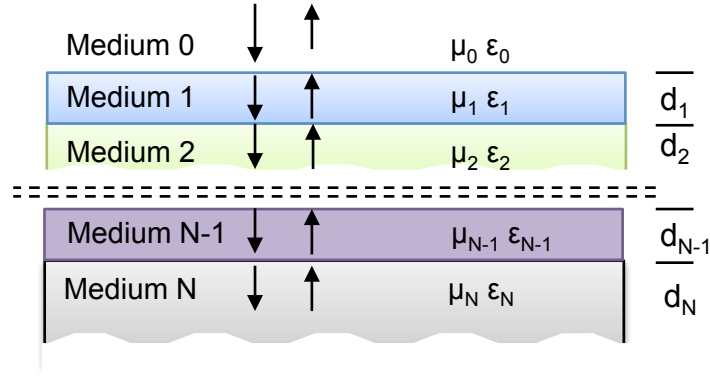


Figure 12 Reflection and Transmission for a multilayer stack of polar thin films

By using the generalized reflective coefficient, it is possible to determine the emissivity of a system consisting of a number of i layers with each having different thicknesses (d_i) and material constants. Therefore, the generalized reflection coefficient is calculated for each interface by determining the known Fresnel reflection coefficient separately and substituting them into the generalized coefficient. In order to calculate the coefficients for the last interface between layer $N - 1$ and N , the process follows the rules for a 2-media system, and thus a generalized reflection coefficient is not needed.

By substituting these constraints for the in-plane wave vector and the reflection coefficient, the adapted formula of the hemispherical emissivity, which is applied for the further calculations, is:

$$\epsilon_\lambda = \frac{\lambda}{4\pi^2} \int_0^{2\pi/\lambda} k_x \sum_{t=TE, TM} (1 - |\tilde{R}_{i,i+1}^{(t)}|^2) dk_x \quad (29)$$

3.3. Implementing in Matlab

The previously introduced equation for the hemispherical is solved numerically by using MATLAB [72]. Therefore one program has been coded, which refers to basically 3 different scripts. The flowchart in Figure 13 has been drawn, in order to visualize the self-written code and how the scripts are called.

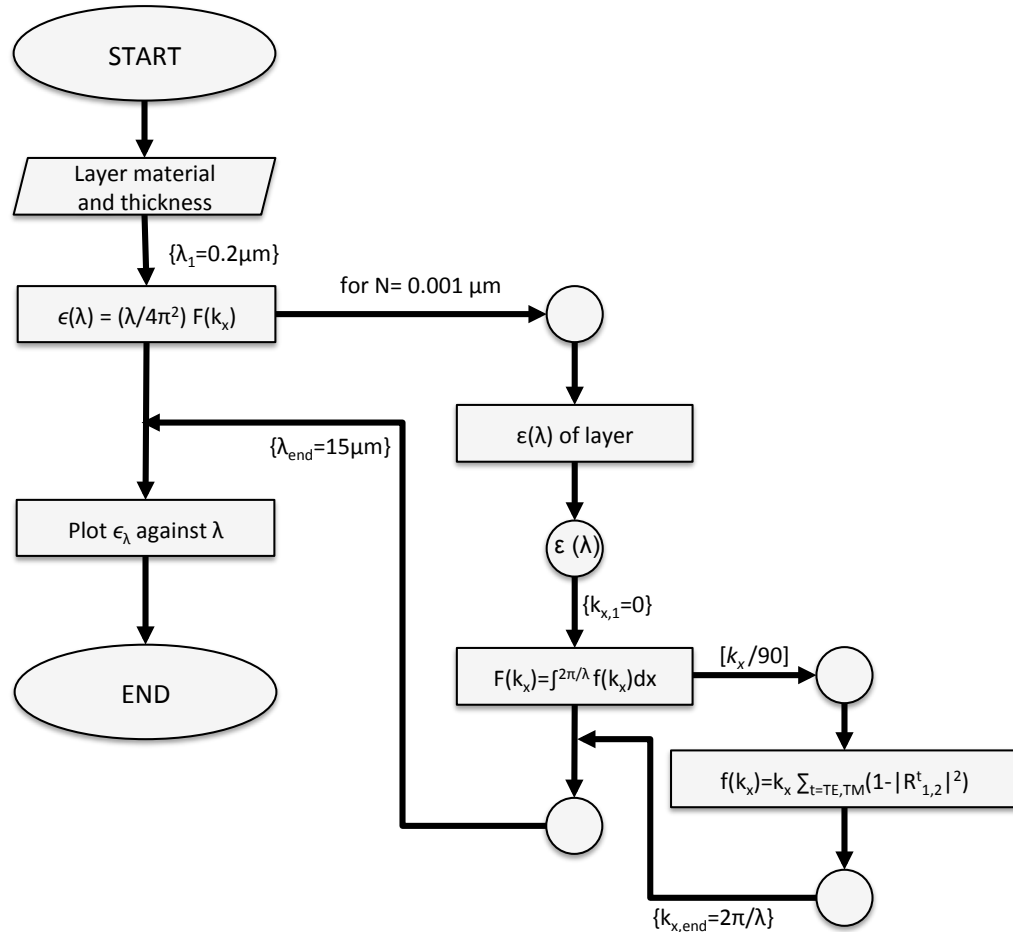


Figure 13 Flowchart of the self-written MATLAB-Code with its subscripts and for-loops

The main program (*MainProgram*) calculates the hemispherical emissivity shown in Eq. 1. Therefore, the thickness of the thin film layer (d) in μm is the only input parameter, which is needed to determine the emissivity for a thin film selective thermal emitter. Additionally, the accuracy of the calculation is defined by the step width of the wavelength and the x-component of wave vector, which represents the incident angles. These step width are also the control variables for the implemented for-loops. They are set as $N = 0.001 \mu\text{m}$ and $n = \frac{2\pi}{\lambda \times 90}$. After choosing a range of wavelengths of interest this program uses for-loops in order to calculate the wavelength depended parameters permittivity and hemispherical emissivity.

In the first step of the for-loop with the control variable N , the dielectric function is determined for the chosen material and saved in the matrix df . This matrix consists of the four columns wavelength, dielectric function, real and imaginary part of the dielectric function, respectively. The permeability is constant over all wavelengths and therefore not included in this matrix. The dielectric function is material dependent and thus it is from a given list in the main program (e.g. df_SiC or df_BN). In this code, each material constant is assigned to a different script, where the specific equation and necessary parameter are already defined. Thus, these scripts are just depending on the wavelength $lambda$.

The second step in the for-loop of the main program is the calculation of the definite integral in Eq. 29. Due to the fact that this integral is not only depending on the wavelength but also on the incident angle, represented by the x-component of the wave vector k (k_x), this loop needs to assign another for-loop in order to calculate the definite integral over all angles for one specific wavelength (spectral hemispherical

emissivity). The script assigned within this for-loop is therefore called “*integr*”. Thus, the main script hands over:

- the layer thickness (d),
- the step width for the wave vector (n),
- the wavelength and corresponding dielectric functions of layer one (thin film) and layer two (high reflective metal), $df1$ and $df2$, respectively
- the permeability of both materials m_1 and m_2 .

Within the for-loop the output variable of the script *integr* is scalar and saved in the variable *Integr*. In order to finally calculate the hemispherical emissivity the result from the Integral is multiplied with $\frac{\lambda}{4\pi^2}$ as described in Eq. 29 and saved in the two-columned matrix *emis* of the form *wavelength | hemispherical emissivity*. Thus, the result of the main program is a matrix consisting of the wavelength and the assigned hemispherical emissivity of the investigated structure.

The already mentioned script “*integr*” determines the Integral of Eq. 29. Therefore, it is divided into two steps. In the first one, another for-loop is implemented in order to calculate the function of the integral in Eq. 29 for each k_x in the interval from 0 to $2\pi/\lambda$. Within this loop, a script called “*f-value*” is assigned and the material-dependent variables ($df1$, $df2$, m_1 , m_2), k_x , the angular frequency (ω) and c , the speed of light are handed over. The output of this is a scalar and is assigned to the control variable k_x in the matrix *fkx* of the form $k_x | fkx$. By the means of the trapezoidal rule, the script “*integr*” determines the definite integral for the above-mentioned function for one specific wavelength. In the end it hands over this scalar to the main program.

Within the script “*f_value*” main part of the calculation is conducted. At first, the wave vector of each layer is calculated by considering the specific permittivity and permeability. By the means of Eq. 9 and Eq. 14 the z-component of each layer is determined by solving: $k_{zi} = \sqrt{\frac{\omega^2}{c^2} \varepsilon(\lambda)_i \mu_i - k_{xi}}$. Since, the investigated structures are opaque, as explained in section 3.1.1, just the generalized reflection coefficient is needed to be determined. Therefore, the Fresnel reflection coefficients, which are depending on the k_{zi} , the material-specific variables as well as the layer thickness (d), are calculated for the TE and TM wave separately at each interface. Then, by the means of the Fresnel reflection coefficients the generalized reflection coefficients for the TE and TM wave are calculated backwards. Assuming the case of one thin film on top of the coated substrate, just one generalized coefficient is calculated for the interface between the vacuum and layer one. In the case of two thin layers on top of the Au coating, two generalized reflection coefficients need to be calculated. At first, a generalized reflection coefficient for the interface between thin layer one and thin layer two have to be calculated ($\tilde{R}_{1,2}^{(t)}$). Then, by means of this reflection coefficient and the Fresnel reflection coefficient of the first interface the generalized reflection coefficient for the interface between vacuum and the first layer can be calculated.

In the end of the script *f_value* these coefficients are plugged in Eq. 29 in order to calculate the spectral hemispherical emissivity ($\epsilon_\lambda(\theta)$), which is then hand over to the script *integr* as the variable *fkx*.

3.4. Simulation and Validation of the introduced material groups

In the following section the simulation and validation of the MATLAB-code is conducted for the three previously introduced material groups. In this study the hemispherical emissivity is calculated as described before. By changing the structure parameter of the investigated selective thermal emitters the findings can be directly influence. These changes can easily be seen and compared by plotting the hemispherical emissivity against the wavelength.

In order to get reliable results from the self-coded program, it is of crucial importance to validate the model. Thus, the results are compared with different publications, which are using the same materials and constraints. In the following section the model for all three material groups will be validated.

Polar materials

At first, the model is tested for the polarized materials, in particular SiC. The polaritonic model determines the dielectric function of SiC shown in Eq. 16. For SiC the parameters ϵ_{∞} , ω_{TO} , ω_{LO} , and Υ are assumed to be 6.7, $9.83 \times 10^{-2} \text{ eV}$, $1.20 \times 10^{-1} \text{ eV}$ and $5.90 \times 10^{-4} \text{ eV}$, respectively. The results, in particular the real and imaginary parts of the dielectric function are plotted in Figure 14.

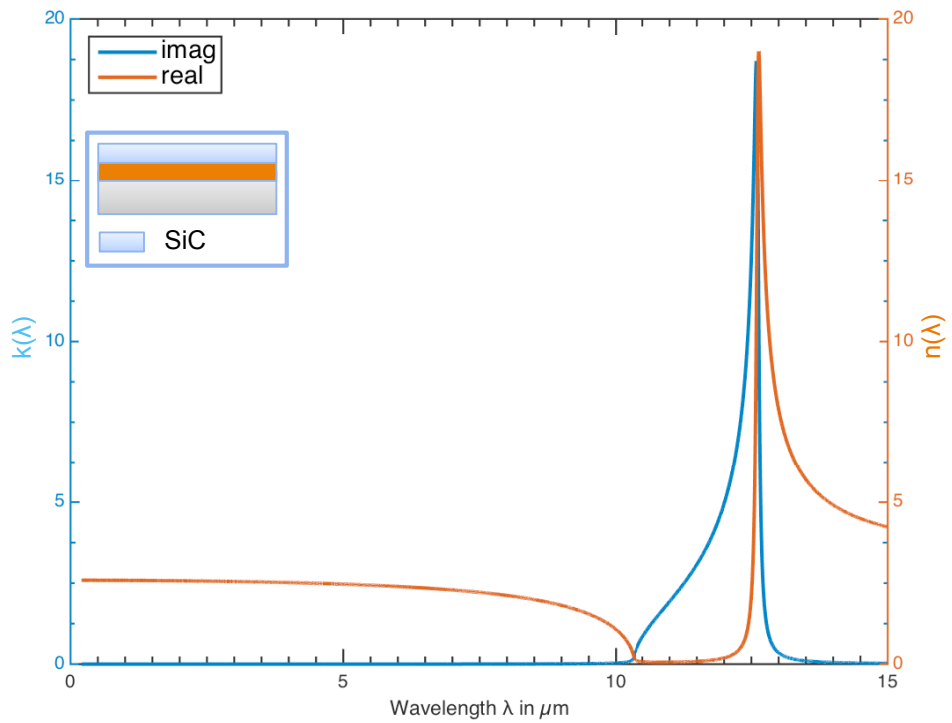


Figure 14 Real and Imaginary parts of the complex dielectric function of SiC

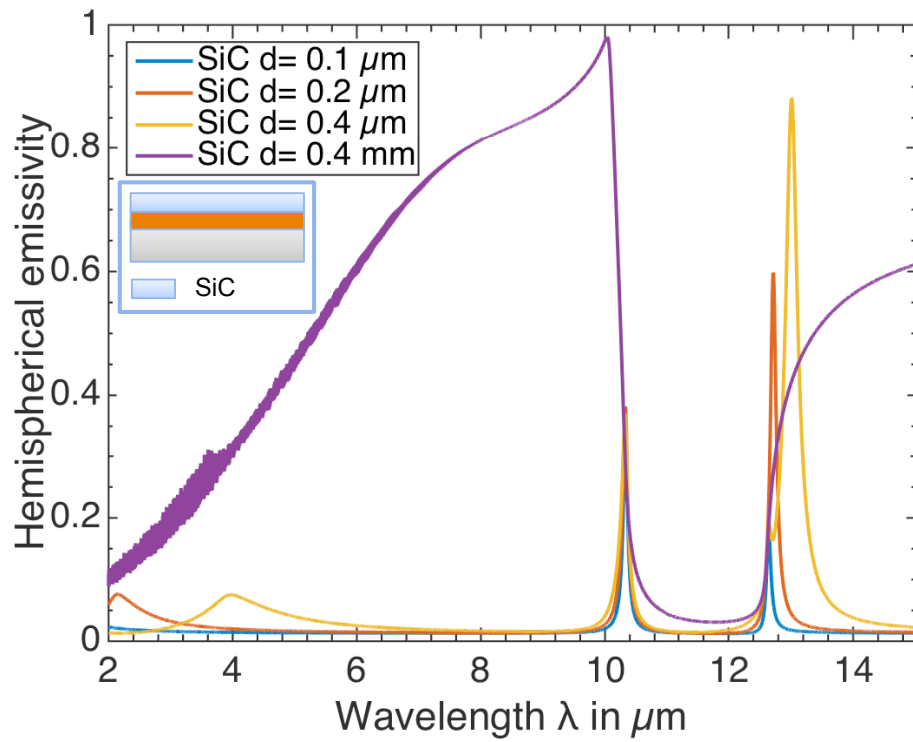


Figure 15 Hemispherical emissivity of SiC thin films on Au-coated substrate for various layer thickness

By applying the Drude model, the dielectric function of Au is determined according to Eq. 22. Therefore, the parameters $\omega_p = 9.06 \text{ eV}$ and $\gamma = 9.06 \text{ eV}$ are used. These values are taken from Johnson and Christy [70].

The emissivity is compared for the thicknesses of $d_1 = 0.40 \text{ mm}$, $d_2 = 0.40 \text{ }\mu\text{m}$ and $d_3 = 0.20 \text{ }\mu\text{m}$. The hemispherical emissivity spectrum for a layer thickness of $d = 0.40 \text{ mm}$ can be assumed to be equal to the emissivity of bulk SiC due to the fact that the absorption depth is less than 0.40 mm. In the range from $\sim 11 \text{ }\mu\text{m}$ to $\sim 13 \text{ }\mu\text{m}$ the emissivity is close to 0, which is called the *Reststrahlen band* [44]. For both of the thin layers (0.2 μm and 0.4 μm) two peaks at approx. 10.5 microns and 13 microns occur. The one at around 13 microns is shifting to high wavelengths with an increasing layer thickness. The first peak occurs to be at the same wavelength as the minimum of the real part of the dielectric function. This wavelength is also called λ_{ZIM} for zero-index material, because the dielectric function would reach zero without dissipation. The second peaks at around 13 microns, occurs to be at the same wavelength as the maximum of the real part n of the refractive index n . The imaginary part k is at a maximum at this wavelength, as well. These presented results are equal with the ones published by Narayanaswamy et al. [44].

Polymer (Polystyrene)

Secondly, the model is tested for the PS and the hemispherical emissivity is plotted in Figure 16.

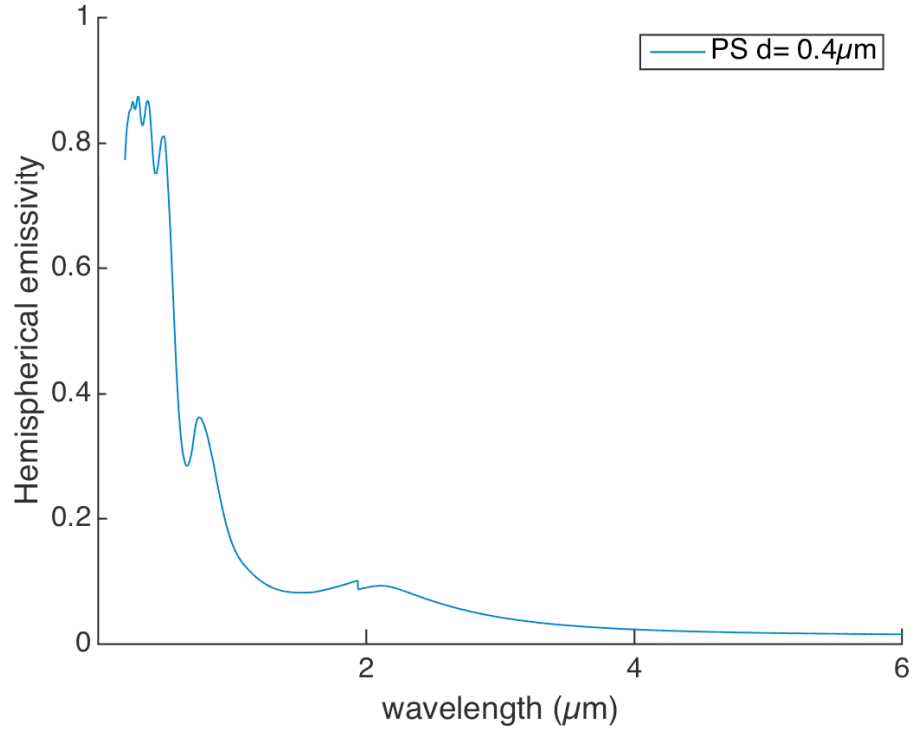


Figure 16 Hemispherical Emissivity of PS thin film on Au-coated substrate for a thickness of 0.4 μm

Here, the dielectric function is approximated by the four-term-fit shown in Eq. 17 and the parameters are given as $f_i = [14.6, 96.9, 44.4, 136.9]$, $\omega_i = [6.35, 14.0, 11.0, 20.1]$ and $g_i = [0.65, 5.0, 3.5, 11.5]$ [67]. These parameters are all in eV . Here, the hemispherical emissivity is plotted for a layer thickness of $d = 0.4 \mu\text{m}$ in the spectral range from 0 microns to 6 microns and compared with the results in Ghanekar et al. [68] In the range from 0.2 microns to approx. 0.7 microns, the emissivity of PS oscillates between 0.75 and 0.85 with a last peak at 0.5 microns and an emissivity of 0.8 before it drops down to an emissivity of 0.3 at 0.6 microns. The second significant peak can be obtained at approx. 0.75 μm . There the emissivity reaches a value of ~ 0.35 before it decreases continuously to a value of 0.1 with a small

shoulder at 2 μm . For higher wavelength the emissivity of PS converges to zero. Ghanekar et al. also calculated these results [68].

Polymer doped with metal nanoparticles

At third, the model for a layer of PS doped with Au NPs is validated. Therefore, the dielectric function of Au is of special interest. As explained before, the permittivity of Au needs to be calculated in two parts: In the range from 0.2 μm to 1.9 μm the complex dielectric function is determined by interpolation the measurements obtained by Johnson and Christy [70]. In addition, the dielectric function for higher wavelengths is calculated by applying Drude model. The resulting real and imaginary parts of the complex permittivity of Au are plotted in Figure 17.

Here, It can be seen that the real and imaginary part in the range from 0.2 μm to approx. 0.5 μm are almost equal. For higher wavelengths the imaginary part is strictly monotonic increasing. In opposite, the real part is almost zero in the range from approx. 0.5 microns to 2 microns. After that, it is also increasing. However, the real part is always significant lower than the imaginary.

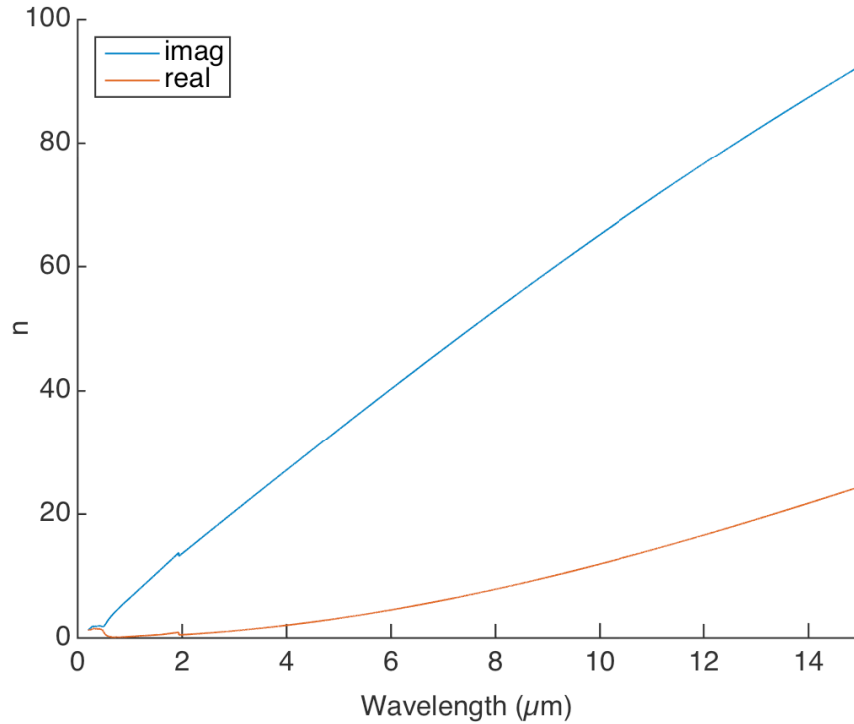


Figure 17 Real and imaginary parts of the complex dielectric function of Au

In order to validate the written code for PS layers doped with Au nanoparticles, the results are compared with the published results in Ghanekar et al. [68]. The thin film of PS with various volume fractions of 0%, 5%, 10% and 30% are presented in Figure 18, where the graph for a volume fraction of 0% correspond to the graph presented in Figure 16.

In order to simulate this hemispherical emissivity with Au nanoparticles, the dielectric function is calculated as described in section 3.2.3, including the size dependence of the nanoparticles. Adding Au nanoparticles to the matrix leads to a decrease of emissivity in the range from 0.2 μm to 0.7 μm. Furthermore, the doped material shows a stronger oscillation between 0.7 μm and 1.0 μm, which can go high as 0.8 and low as 0.35, before it reaches the another maximum at 1.1 μm. However, over all the different volume fractions the oscillating maximum is almost constant.

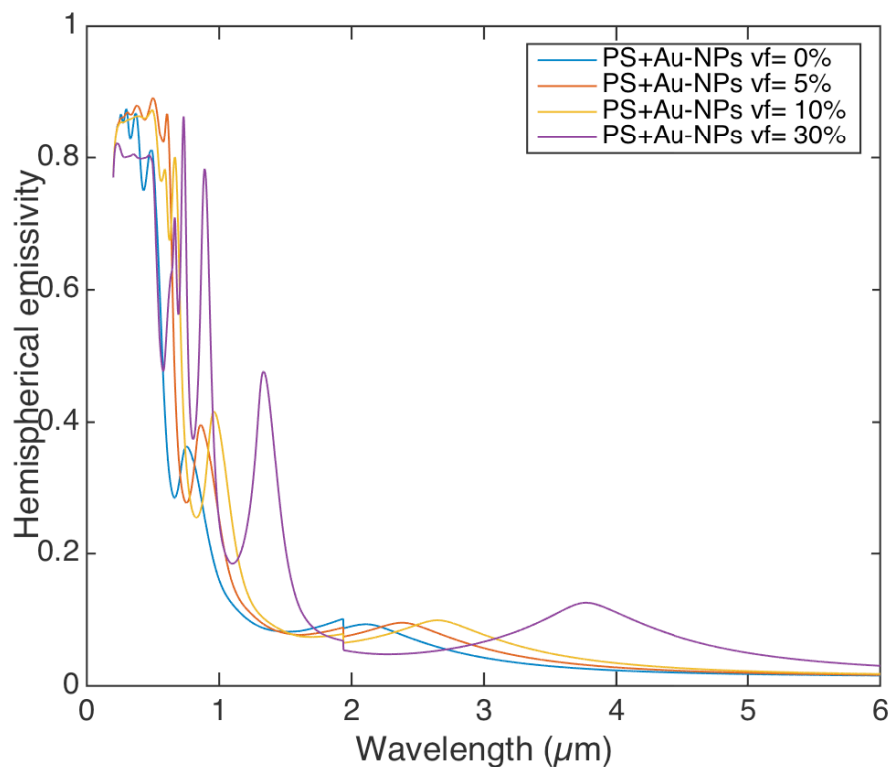


Figure 18 Hemispherical emissivity for PS thin films doped with Au-NPs of various volume fractions (0%, 5%, 10% and 30%)

After reaching this maximum, the emissivity for Au-doped PS also drops down to values of 0.3 or 0.2 for volume fractions of 5% or 30%, respectively. Then, it increases again to a peaks reaching from almost 0.4 to 0.45 for higher volume fractions. The very small peak, which occurs for pure PS to be at around 2.1 μm is slightly increasing with a higher volume fraction. It also can be noticed that this peak is shifting to higher wavelength (e.g. 3.8 μm for 30%). Ghanekar et al. have calculated these results, as well. [68]

3.5. Selectivity of different chemical and biological molecules

In order to design a selective sensing device based on selective thermal emitters, it is of crucial importance to know the optical properties of the target analyte. In particular, the emissivity spectrum (or absorption spectrum) of the analyte has to match the one of the designed emitter. Roughly, the spectral regions of possible analyte can be divided into 2 groups: the visible/near-UV region and the IR region. Table 3 lists a various number of molecules and their specific absorption wavelength(s) or absorption bands.

Table 3 Absorption wavelength of various molecule/materials at room temperature

Molecule/Material	Absorption Wavelength [μm]	Ref.
Ethidium Bromide	0.210 to 0.480	[65]
Ethidium + DNA complex	0.300 to 0.520	[65]
7-hydroxycoumarin (HCM)	0.320 to 0.380	[66]
β -carotene	0.375 to 0.520	[67]
1-Hydroropyrene (1-OHP)	0.388	[68]
Cysteine	0.65 to 0.725	[69]
Hemoglobin (fully oxygenated)	0.70 to 1.05	[71]
2,4,6-trinitrotoluene (TNT)	6.2, 6.4, 7.1 and 7.4	[44]
Polyaniline (PANI)	6.25 to 14.3	[22]
Aromatic C-H Bending	11,6 to 14,7	[71]
Oxonium Hexafluoridosilicate(2-)	13.55, 15.5 and 20.62	[72]

Table 4 Analyte and possible marker material

Analyte	Marker	Ref.
H ⁺ (ph-Sensitive)	Polystyrene/polyacrylamide	[6]
Immunoglobulin	SiO/SiO ₂	[31]
Cysteine & Homocysteine	Cuo/ZnO	[74]

For these values, it has to be noticed, that a characteristic absorption band from 6.25 μm to 14.3 μm (see polyaniline) also includes some maxima and minima, due to the complex structure of the molecules. For example, the vibration of the C=C stretching in the existing quinoid and benzenoid rings cause two peaks at 6.39 microns and 6.79 microns, respectively. Moreover, the C-N stretching in the aromatic ring, the N-quinoid-N stretching vibration are also showing distinct peaks at 7.71 μm and 8.88 μm . However, these peaks are extreme point within the specific absorption band of PANI, whereas the emissivity over the entire band is relatively high [39]. The hemispherical emissivity of TNT also shows four peaks in a spectral range from 6.2 microns to 7.4 microns, but in contrast to PANI, in between these peaks the emissivity is almost zero [51]. Thus, it cannot be called a characteristic absorption *band*, however the peaks still can be interpreted as a unique fingerprint of TNT.

CHAPTER 4 – Results

In order to show that different structures of selective thermal emitters can be applied to detect biological analytes in biological samples, the three material groups and their hemispherical emissivity are analyzed in the following section. Therefore, different plots of hemispherical emissivity are presented. For polar materials different combinations of SiC and BN including thin layers with various thicknesses as well as doped layers are shown. Moreover, the influence of various volume fractions of Au nanoparticles in doped PS is investigated.

4.1. Hemispherical emissivity of various polar material structures

4.1.1. Thin film structures of polar materials

At first the emissivity of polar materials, which in this study are represented by SiC and BN, are investigated. Initially, the hemispherical emissivity is calculated for thin films of both materials on Au-coated Si substrate. Based on these results a first assumption on how the emissivity is influenced by the materials can be made.

Figure 19 shows the hemispherical emissivity of BN for different layer thicknesses ($d=[0.1, 0.2, 0.4,] \mu\text{m}$). The thin films of BN have two distinct emissivity peaks, one at approx. $7.5 \mu\text{m}$ and at approx. $9.5 \mu\text{m}$. The peak at $7.5 \mu\text{m}$ is slightly increasing with a thicker layer of BN. However, varying the thickness leads to significant change for the second peak. By doubling the thickness from $d=0.1 \mu\text{m}$ to $d=0.2 \mu\text{m}$ this peak occurs to be as twice as high. Additionally, this peaks is slightly

shifting to a higher wavelength. For a layer thickness of 0.4 microns, the peak is marginally smaller than the one for $d=0.2\ \mu\text{m}$. However, there occurs an additional peak at the same wavelength as the one for $d=0.1\ \mu\text{m}$, which is connected with the main peak at approx. 10 microns. Between all the peaks, the emissivity is very close to zero, which is due to a high reflectivity at these wavelengths (see Kirchhoff's Law and Eq. 23).

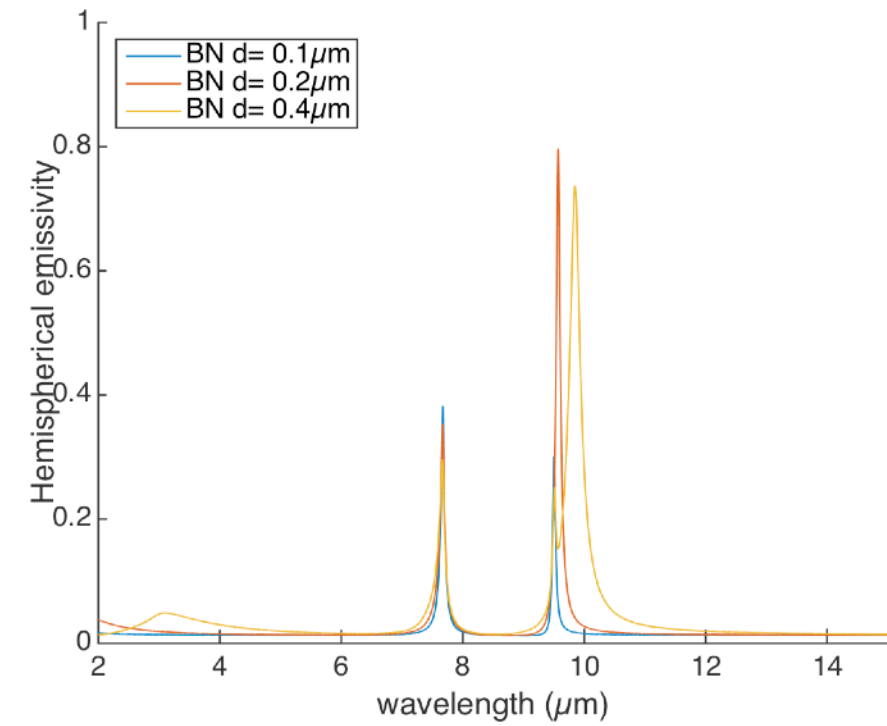


Figure 19 Hemispherical emissivity of BN thin films on Au-coated substrate for various layer thickness

Considering the hemispherical emissivity for SiC from Figure 15, which shows a very similar behavior regarding the increasing layer thickness, one could assume that this is a general law for polar materials. However, to proof this assumption more materials have to be analyzed.

4.1.2. Doped polar material

In the next step, both materials are combined in order to form a doped layer on top of the Au layer. Therefore, the particle size is set to be 25 nm in diameter and the volume fraction of particles in the matrix is varied from 10% to 30% in three steps.

Doped SiC thin films

Figure 20 shows the calculated emissivities of different structures of SiC-doped BN matrix with a thickness of $0.4\mu\text{m}$ each. Additionally, the emissivity for thin films of pure SiC and BN of the same thickness are shown as a reference.

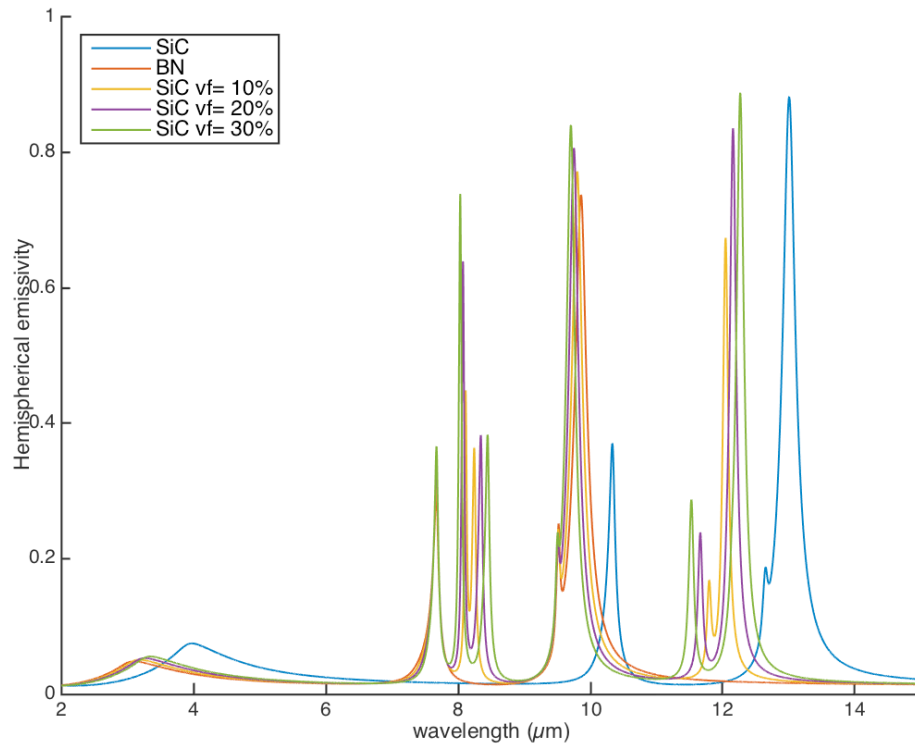


Figure 20 Hemispherical emissivity for SiC thin films doped with BN-NPs of various volume fractions (10%, 20% and 30%)

In this figure, the emissivity peak of BN, which originates from the TM wave, is slightly increasing with a higher volume fraction of SiC nanoparticles. The behavior is

comparable with the one for pure BN thin films, where the same peak is increasing, by decreasing the layer thickness from 0.4 μm to 0.2 μm . Furthermore, four more peaks can be seen in this Figure 20. Two are at 8.0 microns to 8.5 microns, which are connected. Together with the one for the BN thin film they form a trident. Additionally, they are more peaks, which can be identified at 11.9 microns and 12.1 microns for a volume fraction of 10%. These two peaks are shifting slightly away from 12 microns with an increasing volume fraction. The smaller one shifts closer to 11.5 μm and the higher one to 12.5 μm . However, both new peaks are the fusion of the peaks known from the thin film structures. This is underlined by the fact that with an increase in the volume fraction, these peaks are diverging towards the peaks of pure BN or SiC thin films, respectively.

Doped BN thin films

Furthermore, selective thermal emitters with different structures of SiC matrix doped with various volume fractions of BN nanoparticles are simulated. In Figure 21, these results are plotted as well as the hemispherical emissivity for SiC and BN thin films of 0.4 microns each. In opposite to the pure thin films, the BN-doped SiC shows four more peaks. They can be identified at approx. 8.5 microns and 9.0 microns as well as at approx. 11.0 microns and 11.5 microns. With an increasing volume fraction of BN nanoparticles, the first two are slightly diverging from 8.5 microns towards 8.0 microns or 9.5 microns, respectively. The maximum of the smaller one is almost constant at 0.4, while the maximum for the second one is increasing from 0.7 to 0.9.

Additionally, the interaction between BN-nanoparticles and SiC matrix leads to two more peaks at approx. 11.5 μm . These peaks show a similar behavior as ones for a

shorter wavelength. With a volume fraction of 10 % they are very close to each other at 11.5 μm , but with an increasing percentage of BN nanoparticles they are diverging to either 11.0 μm or 12.0 μm . Moreover, the higher increases from 0.45 to its maximum at 0.8 with the volume fractions of 10% and 30%, respectively. The smaller one is almost constant at approx. 0.25 for the simulated volume fractions.

Furthermore, this combination of BN and SiC also shows two new peaks, which are a fusion of the peaks originating from the thin film structures of pure polar materials. Additionally, they are diverging towards the thin-film-peaks.

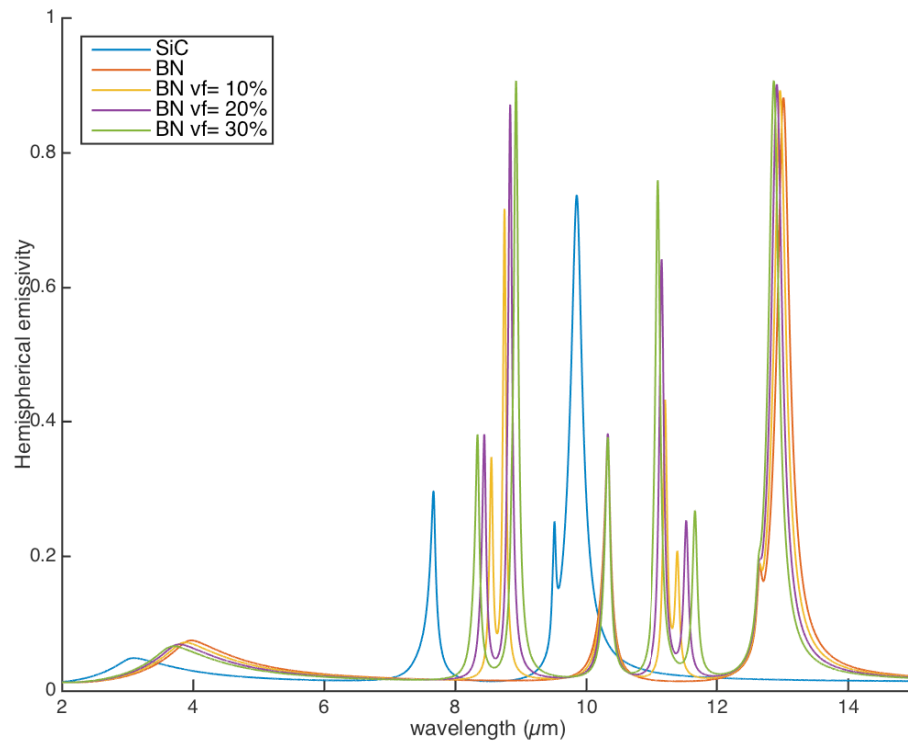


Figure 21 Hemispherical emissivity for BN thin films doped with SiC-NPs of various volume fractions (10%, 20% and 30%)

Considering the simulations of selective thermal emitters structures of BN matrix doped with SiC nanoparticles and vice versa, some similarities can be identified: In both cases the peaks known from thin film structures are almost not changing with added nanoparticles. However the added nanoparticles lead to interactions, which create new peaks in between those known from pure thin films. With an increasing volume fraction these peaks are diverging towards the thin film peaks. As it can be seen in Figure 22, depending on the material, which is forming the matrix, the new peaks are at different wavelength. Thus, hemispherical emissivity peaks can be created by varying the composition of SiC and BN at around every $0.5 \mu\text{m}$ in the range between $7.5 \mu\text{m}$ and $13 \mu\text{m}$.

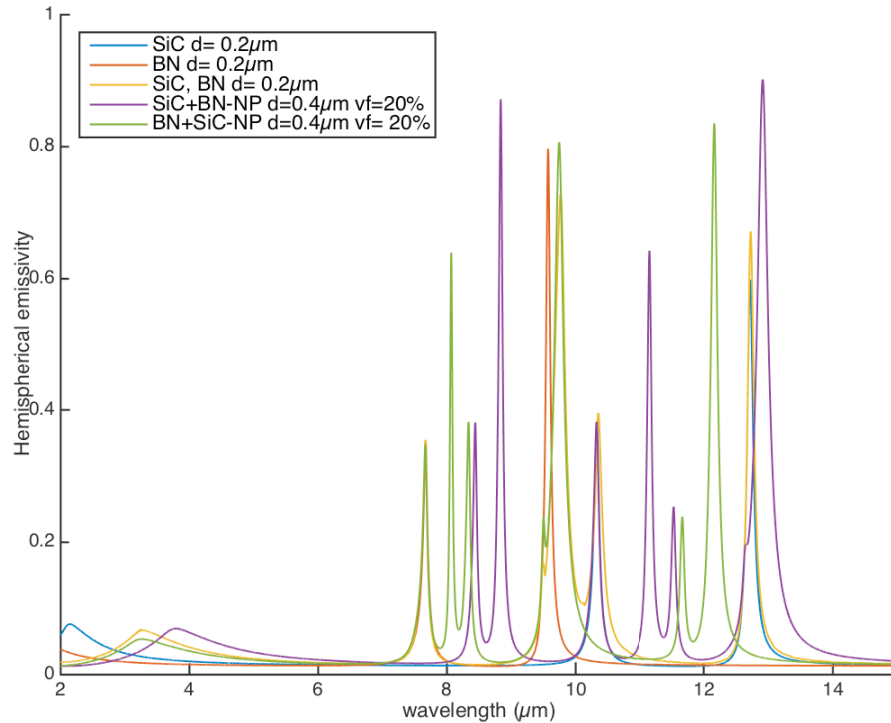


Figure 22 Hemispherical emissivity for various combinations of SiC and BN

4.2. PS doped with Au nanoparticles

In the following, the hemispherical emissivity of selective thermal emitters consisting of a PS layer doped with Au nanoparticles is simulated. The particles size is set to be 25 nm in diameter and the volume fraction is varied from 0% to 50% in steps of 5%. Figure 23 shows the spectral emissivity results for doped PS thin films of a layer thickness of $d = 0.40 \mu\text{m}$. The volume fraction varies from 0% to 50% in steps of 10% due to the readability. In the appendix (A1) the hemispherical emissivity is presented for volume fractions from 0% to 50% in steps of 5%. However, the trend is also recognizable in Figure 23.

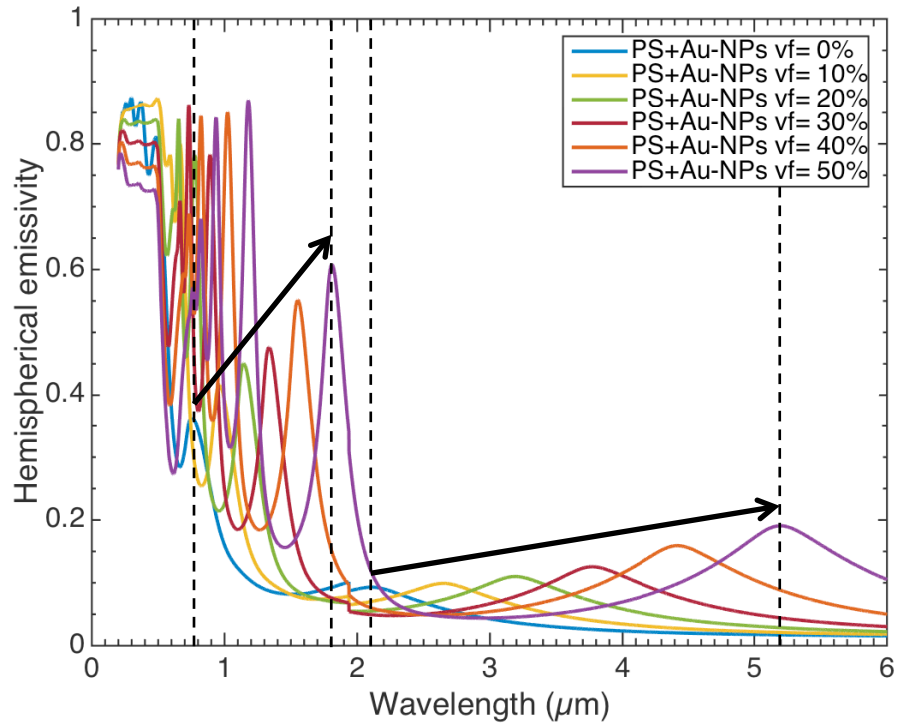


Figure 23 Hemispherical emissivity of a PS thin layer ($d=0.40 \mu\text{m}$) doped with various volume fractions of Au nanoparticles ($r=25 \text{ nm}$)

As a result, a characteristic curve profile can be noted for all volume fractions. This profile starts with an emissivity at around 0.77 and reaches a small plateau afterwards (0.2 microns to 0.6 microns). Then, the curve starts oscillating and reaches a first single peak before it drops down to a minimum. Right behind that minimum it increases to another peak before it decreases to an emissivity of approx. 0.05. With increasing wavelengths the curves reach another noticeable peak with a small absolute value but a wider range.

However, it can be noticed that the absolute value of the plateau is decreasing for increasing volume fractions. In particular it is reduced from 0.87 to 0.74 for volume fractions of 0% and 50%, respectively. Moreover, the oscillation gets also stronger for higher percentage of Au nanoparticles. It drops down to values of 0.4 and 0.3 for 40% and 50%, respectively. Nevertheless the maximum of this oscillation is almost constant over all volume fractions. It is approx. 0.85.

Furthermore, the curves minimum is shifted to higher wavelengths with a higher number of Au nanoparticles in the matrix. In addition, it is decreasing by 50% from 0.3 to 0.15. At the same time the next peak is significantly increasing and shifting to higher wavelengths from around 0.3 at $\lambda = 0.6 \mu m$ to 0.6 at $\lambda = 1.8 \mu m$. Moreover, the small peak at wavelengths higher than 2 microns is continuously shifting with increasing volume fractions to higher wavelengths. This peak for a volume fraction of 50% has a absolute value of 0.18 at a wavelength of 5.2 microns, which is just slightly higher than the one for 20% at 2.1 microns (+0.08).

In general, the emissivities in Figure 23 show that an increasing volume fraction is shifting the peaks to longer wavelengths as well as to higher maxima and smaller

minima. In addition, it can be noticed that the second peak is stronger increasing than shifting whereas the third and last peak shows a stronger shifting and just a small increase in the absolute values.

The curves for a changing volume fraction from 0% to 50% in steps of 5% are plotted in Figure 24 and Figure 25. According to the introduced approach in Figure 9, by comparing the resulting curves they can be used in order to analyze how the analytes from the sample react with the nanoparticles in polystyrene.

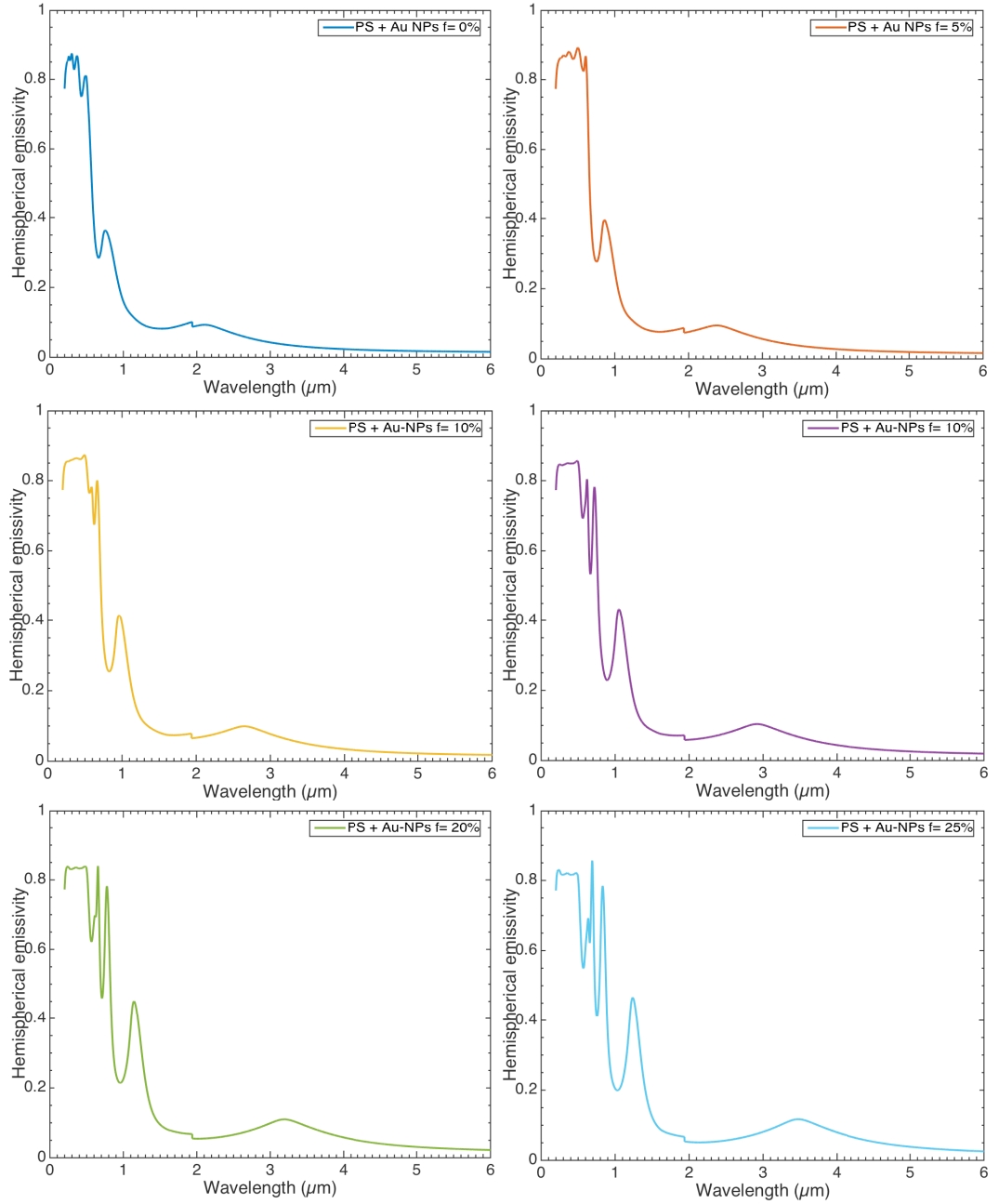


Figure 24 Hemispherical emissivity of a Polystyrene layer doped with Au nanoparticles with various volume fraction from 0% to 25%

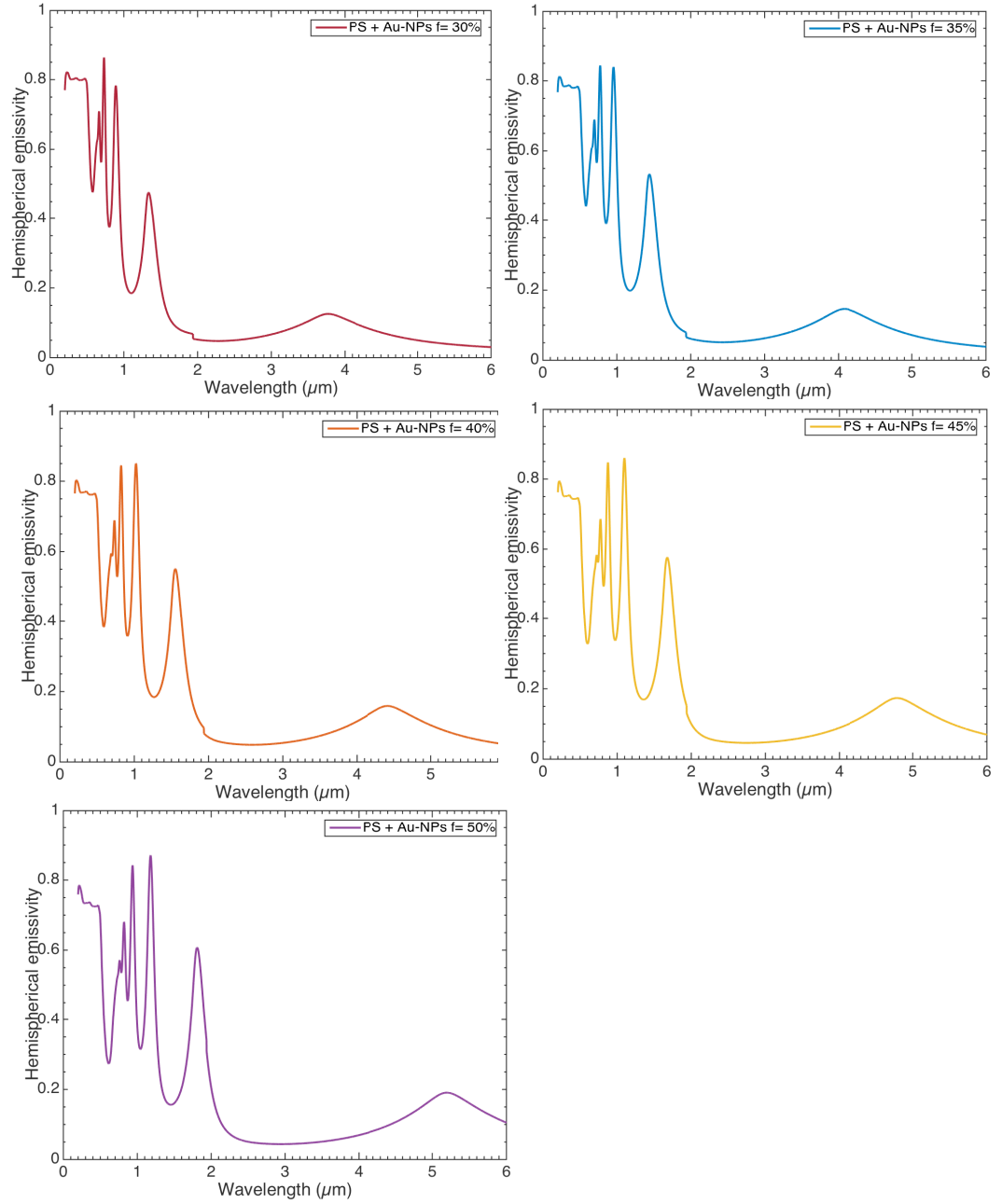


Figure 25 Hemispherical emissivity of a Polystyrene layer doped with Au nanoparticles with various volume fraction from 30% to 50%

4.3. Evaluation of Results

In this section, the results of the foregoing simulations are compared regarding their capability of forming optical biosensors in the visible/near-UV spectrums as well as in the IR spectrum. The various combinations of polar materials as thin layers as well as doped materials, offer a wide application area in the IR spectrum. Depending on which material (SiC or BN) is used to form the matrix, doping this material with nanoparticles of the other materials creates new peaks of emissivity at different wavelength. In this study the scope of applied polar materials is limited to SiC and BN. However, the combinations of these materials create emissivity peaks at every 0.5 μm in the spectrum between 7.5 μm and 13 μm .

In addition, Figure 26 shows that it is also possible to design Au-doped PS emitters, which could detect molecules in the visible/near-UV spectrum due to a additional absorption. This absorption occurs in a range from 0.3 μm to 0.7 and is caused by the presence of the Ethidium-DNA complex. Using a volume fraction of 5% the selective thermal emitter provides a high absolute emissivity, which would be reduced due to an additional absorbance. Furthermore, increasing the volume fraction up to 10%, this emitter would be useful in order to investigate fully oxygenated Hemoglobin in the range from 0.71 microns to 1.05 microns.

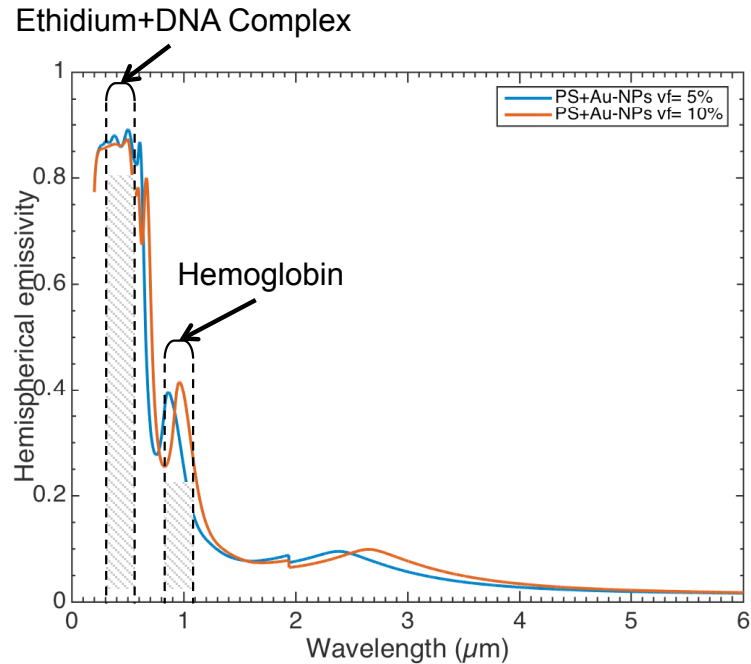


Figure 26 Matching emissivity spectrum of PS thin layer doped with Au nanoparticles and absorption bands of Ethidium w/ DNA complex and Hemoglobin

4.4. Experimental measurement

Besides theoretical calculations, experimental measurements of different structures are of crucial importance in order to verify the properties and transfer them into practical applications. In order to conduct the measurement three selective thermal emitter samples, which have been fabricated by Prof. H. Sun and H. W. Su. from Umass Lowell, are investigated. These emitters consist of a multilayer structure on top of an Au-coated Si substrate. The first layer is made of SiO₂ and its thickness is varied ($d_1 = [0.2, 0.6, 1.0] \mu m$). In between this layer and the coated substrate a thin layer of PS is deposited. Its layer thickness is constant for all three samples ($d_2 = 0.3 \mu m$). A picture of these samples has been taken before the FTIR measurement and is shown in Figure 27.

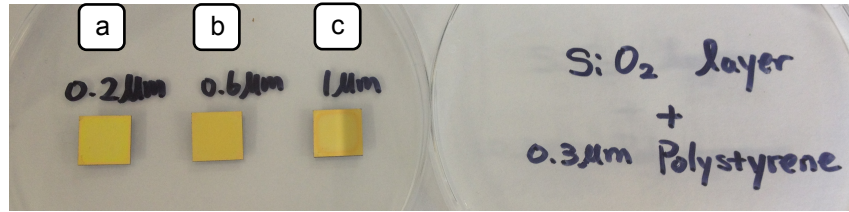


Figure 27 Selective thermal emitter samples with multilayer design (SiO₂ - PS - Au)

4.4.1. Fabrication of samples

The samples are fabricated within three steps as shown in Figure 28. In the first step an Au layer with a thickness of 1 μm is deposited on a Si substrate by using electron beam deposition (EBD). EBD is an inexpensive way to create surfaces and coatings of different sizes, which has unique advantages in precision in micron in particular in nanoscale applications that enables the application for several research fields. However, it is a time-consuming, direct-writing technique, which is not suitable for mass fabrication [81]. In order to coat the sample substrate with a thin Au layer, the Si substrate is mounted on rotor in the upper side within a vacuum chamber. An Au sample, the target, is placed on the other side of the chamber. The applied high-energy electron beam is focused on the target. Due to the high kinetic energy, which is immediately transformed into thermal energy when the electron beam strikes the surface. This heat is vaporizing the target's surface. Then, the Au atoms are deposited on the Si substrate due to the electronic potential [82] [83] [84].

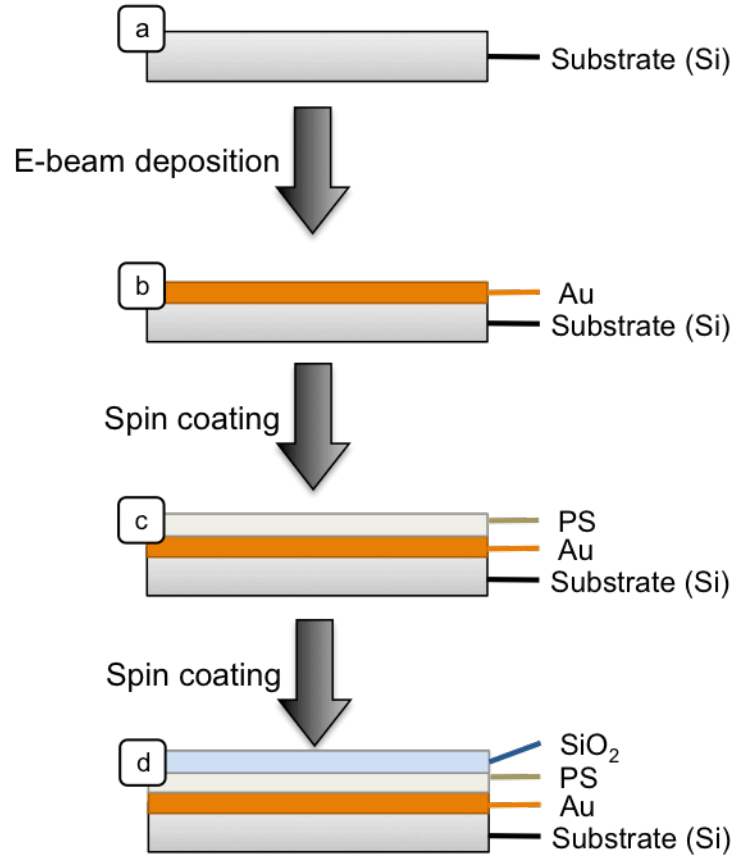


Figure 28 Fabrication process of multilayer samples (SiO₂ - PS - Au - Si)

In the second and third step, the thin films of PS and SiO₂ are deposited with spin coating. Spin coating is a frequently used technique to fabricate high quality thin films in small scale and research purposes. It has advantages in process handling, due to its easy, fast and reproducible characteristics. Moreover, it enables the preparation of uniform and well-integrated nanolayers.

The spin coating process, is divided into four steps: solution deposition, spin-up, spin-off and film drying, which all have an influence on the quality of layer deposition. In order to coat the sample with an Au-doped PS layer, a solution of PS including Au nanoparticles is dropped onto the Au-coated substrate, which is mounted

onto a rotor. Due to the following rotation the solution is distributed equally over the surface (spin-up) and with an increasing, ongoing rotation the surplus solution is spun off. These spinning steps define the thickness and distribution of the solution in the layer. In the last step, the sample is dried and results in the finished sample [85] [86] [87].

4.4.2. Results FTIR spectroscopy

FTIR spectroscopy

After the three samples are fabricated as explained in section 0, their hemispherical emissivity is measured using FTIR spectroscopy. This method is taking advantage of the fact that each peak in an infrared spectrum depends on a certain molecule structure. Thus, it is commonly applied as chemical analysis of different molecules and their concentration in samples. These samples can be in various states, such as solid, crystal, film etc. [88].

They are different way to design these interferometers. However the basic principle is the same: Light from an IR source is reflected by a several mirrors, which split and recombine the beam in order to finally reflect the beam by the means of a parabolic mirror towards the sample. There it interacts with the sample and the interferogram is detected. This interferogram is Fourier transformed into an infrared spectrum [89].

There are tow methods, which can be applied in order to obtain the hemispherical emissivity using FTIR spectroscopy. The direct method measures the radiation of the sample and compares it with the blackbody radiation to generate the emissivity

spectrum. The indirect method is measuring the transmission and reflectivity of the sample in order to generate the emissivity spectrum [90].

In this study, the indirect method is applied to measure the emissivity spectrum of the SiC-doped PS layer. Therefore, the Attenuated Total Reflectance (ATR) method is applied. In order to conduct the measurement, the sample is mounted onto a germanium (Ge) crystal with close contact. The IR beam is coming from below the crystal. The high refractive index of Ge leads to an internal reflection, which generates an infinitesimal wave. This is interacting with the sample and then reflected back towards the detector.

Analysis of the samples

The results of the FTIR measurements for the three fabricated selective thermal emitters are presented in Figure 29. All three samples show a similar characteristic curve in the IR spectra. In the range from 2 microns to 8 microns they show no emissivity spectrum. At a wavelength of 8 μm the emissivity strongly increase until it reaches a maximum at approx. 8.4 μm for a SiO_2 layer of 0.2 μm thickness. This maximum is slightly shifting to higher wavelengths with the thicker top layers of SiO_2 . Then the emissivity decreases to a first minimum at around 9.8 μm for $d_1 = 0.2 \mu\text{m}$, but slightly shifting to smaller wavelength for the other samples. Directly behind that minimum a very small increasing emissivity can be noticed for SiO_2 layers of 0.2 and 0.6 μm thickness.

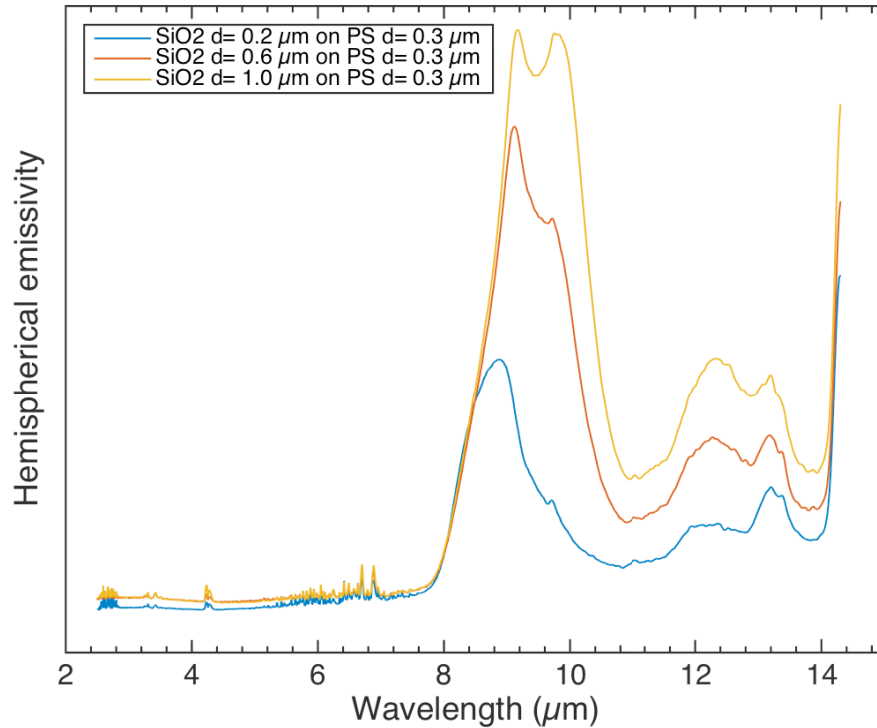


Figure 29 Results from the experimental FTIR spectroscopy

In opposite to these samples, the third sample shows a clear difference to the foregoing minimum. Again, this small peak is shifting to higher wavelengths. At around 10 microns the emissivity significantly drops to the second minimum at approx. 11 microns. At 11.8 μm the emissivity increases again an absorption band between 12 microns and 14 microns with two significant maxima at 12.2 μm and 13.2 μm . For all the three layer it can be stated, that a thicker layer of SiO_2 leads to higher absolute values over the entire spectrum from 2 μm to 14 μm . Moreover, the maxima are shifting to higher wavelengths with an increasing thickness.

In comparison to these measurements, the Figure 30 shows the calculated hemispherical emissivities for the same structure. First of all it has to be noticed, that the calculated curve for the first sample with a thickness of 0.2 μm is very similar to

the hemispherical emissivity of a single thin film of SiO₂. So it can be assumed that the effect of the PS is neglected in the theoretical model whereas it apparently has significant influence in the reality.

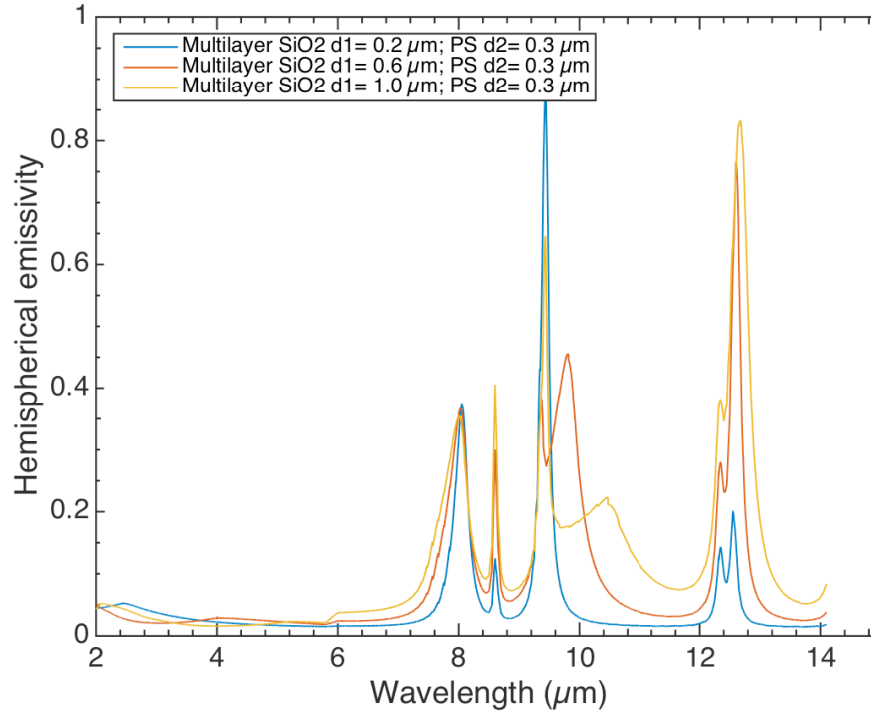


Figure 30 Simulated hemispherical emissivity of a multilayer structure consisting of a SiO₂ thin film on a PS thin film

Furthermore, the curves for samples 1 and 2 look quite different on the first view. However, both graphs for $d_1 = 0.6 \mu\text{m}$ and $d_1 = 1.0 \mu\text{m}$ show some significant similarities with the measurements. First of all, it has to be noticed, that these graphs cannot be compared quantitatively due to the different absolute values on the y-axes. However, the calculated curve for all samples show an increasing emissivity at 8 microns, which is the same as in the measurements. In difference to the measurements, it drops immediately after it reaches a peak at 8 μm before it increase again to the sharp peak at 8.4 microns. At the same wavelength ($\sim 9.3 \mu\text{m}$) as in Figure 29, the curves reach a maximum as a part of the absorption band between approx. 9.2 microns

and 10.2 microns or 11 microns for sample 2 and 3, respectively. In between 11 microns and 12 microns the curves in both figure drop to a minimum before they reach another emissivity peak at approx. 12 μm , which is sharp for the calculation and wide for the measurements.

Although, the obtained results from the samples show a quite different emissivity spectrum, which show not such sharp peaks as the calculation predicted. However, the significant peaks in the hemispherical emissivity spectrum of SiO_2 can be confirmed.

CHAPTER 5 – CONCLUSION

In this study, different structures of selective thermal emitter designs and their hemispherical emissivity spectrum have been analyzed. The goal was to show that selective thermal emitters have the potential to be applied as biosensors in order to detect analytes in biological samples due to their unique radiation properties.

Initially, an insight into the biosensors has been given. This includes the general functionality of biosensors as well the different detection principles. Additionally, several applications of these principles have been introduced, as well. Moreover, the working principle of selective thermal emitters and their application in thermo photovoltaic systems has been given.

Furthermore, a detection method combining both functionalities has been introduced. In order to prove this theory, a MATLAB code has been written using the physical principles of thermal radiation. Based on these principles the hemispherical emissivities of three different material groups: polar materials, PS (polymer), and PS doped with Au-nanoparticles have been simulated.

These materials have been analyzed regarding their influence on the emissivity due to variations of layer thicknesses of thin film applications as well as various volume fractions of doped materials. It can be stated that the characteristic emissivity spectra, for the investigated polar materials SiC and BN, lies in the IR spectrum from 7.0 μm to 13 mm. In opposite to that, the spectra for Au-doped PS thin layers lies in the visible/near-UV range from 0.2 μm to 2.0 μm . In addition, it has been shown that

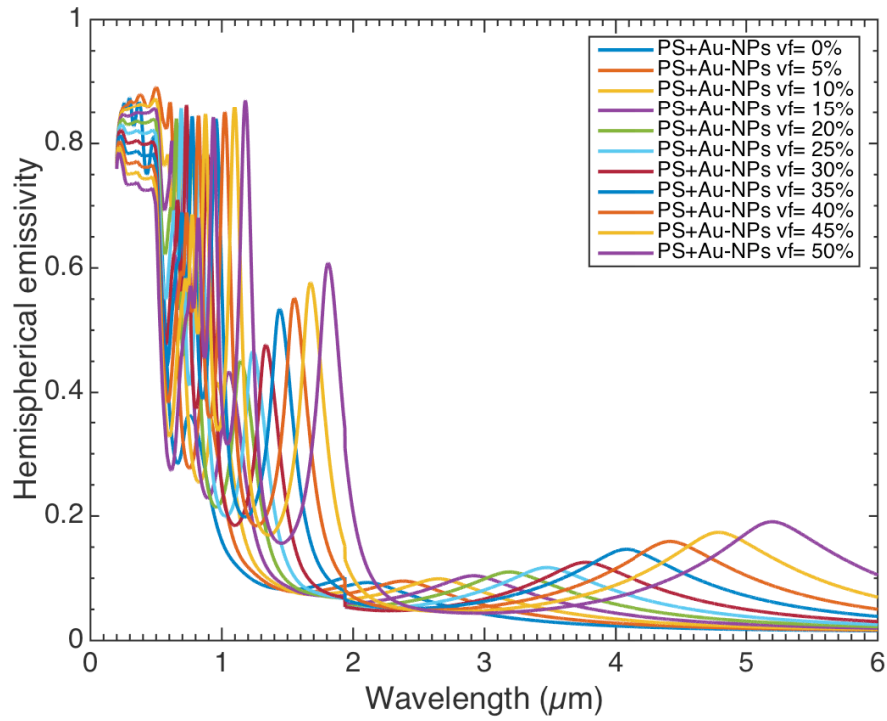
changes in layer thickness as well as in volume fraction of nanoparticles lead to shifts and partly increases of emissivity peaks.

The results of the analysis have been compared to certain molecules and chemical compounds, which have their specific absorption spectra either in the IR or in the visible/near-UV range. It could be shown that these spectra match with the ones from the simulated selective thermal emitters and therefore, their presence could be detectable.

Furthermore, samples consisting of a multilayer have been experimentally investigated. The obtained results from FTIR measurement differ from the calculated ones regarding the absolute value and the sharpness of the emissivity peaks. However, the unique shapes of the curves, which are necessary in order to detect specific molecule in a sample, have been confirmed. All in all, this study has shown that a detection of biological molecule or chemical compounds by means of selective thermal emitters and their unique spectrum of emissivity could be possible.

APPENDICES

A1 Hemispherical emissivity of a PS thin film layer doped with various volume fractions of Au nanoparticles. Layer thickness is 0.4 μm on top of a Au coated Si substrate



BIBLIOGRAPHY

- [1] J. S. Daniels and N. Pourmand, "Label-Free Impedance Biosensors: Opportunities and Challenges," *Electroanalysis*, vol. 19, no. 12, March 2007.
- [2] A. Benvidi et al., "a highly sensitive and selective electrochemical DNA biosensor to diagnose breast cancer," *Journal of Electroanalytical Chemistry*, vol. 750, pp. 57-64, May 2015.
- [3] D. Huo, Y. Xu, C. Hou, M. Yang, and H. Fa, "A novel optical chemical sensor based AuNR-MTPP and dyes for lung cancer biomarkers in exhaled breath identification," *Sensors and Actuators B: Chemical*, vol. 199, pp. 446-4556, April 2014.
- [4] A. Raamanathan et al., "Programmable Bio-Nano-Chip Systems for Serum CA125 Quantification: Towards Ovarian Cancer Diagnostics at the Point-of-Care," *Cancer Prev Res*, vol. 5, no. 5, pp. 706-716, May 2012.
- [5] S. Chakravarty et al., "Multiplexed specific label-free detection of NCI-H358 lung cancer cell line lysates with silicon based photonic crystal microcavity biosensors," *Biosensors and Bioelectronics*, vol. 43, pp. 50-55, November 2012.
- [6] C. Fenzl, T. Hirsch, and O. S. Wolfbei, "Photonic Crystals for

- Chemical Sensing and Biosensing," *angewandte Chemie - International Edition*, vol. 53, pp. 3318-3335, 2014.
- [7] J. J. Talghader, A. S. Gawarikar, and R. P. Shea, "Spectral selectivity in infrared thermal detection," *Light: Science & Applications*, vol. 1, pp. 1-11, August 2012.
- [8] A. P. F. Turner and I. Karube, *Biosensors: Fundamentals and Applications*. Oxford, UK: Oxford University Press, 1987.
- [9] D. R. Thevenot, K. Toth, A. Durst, and G. S. Wilson, "Electrochemical Biosensors: Recommended definitions and classification," *Pure Appl. Chem.*, vol. 71, no. 12, pp. 2333-2348, 1999.
- [10] K. A. Marx, "Toward Understanding the intelligent Properties of Biological Macromolecules - Implications for their Design into Biosensors," in *Smart Biosensor Technology*. Rochester, New York, USA: CRC Press, 2007.
- [11] K. Schügerl, "Progress in monitoring, modeling and control of bioprocesses during the last 20 years," *Journal of Biotechnology*, vol. 85, pp. 149-173, 2001.
- [12] J. Halamek, M. Hepel, and P. Skladal, "Investigation of highly sensitive piezoelectric immunosensors for 2,4-dichlorophenoxyacetic acid," *Biosensors & Bioelectronics*, vol. 16, pp. 253-260, 2001.
- [13] L. D. Mello and L. T. Kubota, "Analytical, Nutritional and Clinical

- Methods: Review of the use of biosensors as analytical tools in the food and drink industries," *Food Chemistry*, vol. 77, pp. 237-256, 2002.
- [14] A. Logrieco, D. W. M. Arrigan, K. Brengel-Resce, P. Siciliano, and I. Tothill, "DNA arrays, electronic noses and tongues, biosensors and receptors for rapid detection of toxigenic fungi and mycotoxins: A review," *Food Additives and Containments* , vol. 22, no. 4, pp. 335-344, 2005.
- [15] S. Rodriguez-Mozaz, M. J. Lopez de Alda, and D. Barcelo, "Biosensors as useful tool for environmental analysis and monitoring," *Analytical Bioanalytical Chemistry*, vol. 386, pp. 1025-1041, 2006.
- [16] X. Jiang et al., "Immunosensors for detection of pesticide residues," *Biosensors and Bioelectronics*, vol. 23, pp. 1577-1587, 2008.
- [17] H.-M. Haake, A. Schütz, and G. Gauglitz, "Label-free detection of biomolecular interaction by optical sensors," *Fresenius Journal of Analytical Chemistry*, vol. 366, pp. 576-585, 200.
- [18] P. D'Orazio, "Biosensors in clinical chemistry," *Clinica Chimica Acta*, vol. 334, pp. 41-69, 2003.
- [19] G. Schaller, K. Evers, S. Papadopoulos, A. Ebert, and H. Bühler, "Current use of Her-2 tests," *Annals of Oncology*, vol. 12, pp. 97-100, 2001.
- [20] A. Poscia, D. Messeri, D. Moscone, F. Ricci, and F. Valgimigli, "A

- novel continuous subcutaneous lactate monitoring system," *Biosensors and Bioelectronics*, vol. 20, pp. 2244-2250, 2005.
- [21] G. Gauglitz and P. B. Luppä, "Point-of-Care-Testing Patientennahe Labordiagnostik," *Chemie in Unserer Zeit*, vol. 43, pp. 308-318, 2009.
- [22] A. Warsinke and Point-of-Care testing of proteins, "Analytical Bioanalytical Chemistry," vol. 393, pp. 1393-1405, 2009.
- [23] S. Hahn, S. Mergenthaler, B. Zimmermann, and W. Holzgreve, "Nucleic acid based biosensors: The desires of the user," *Bioelectrochemistry*, vol. 67, pp. 151-154, 2005.
- [24] A. Sassolas, B. D. Leca-Bouvier, and L. J. Blum, "DNA Biosensors and Microarrays," *Chemical Reviews*, vol. 155, pp. 206-222, 2008.
- [25] F. Scheller and F. Schubert, *Biosensoren*. Basel, boston, Berlin, GER: Birkhäuser Verlag, 1989.
- [26] C. Boozer, G. Kim, S. Cong, and HW. Londergan, T. Guan, "Looking towards label-free biomolecular interaction analysis in a high-throughput format: a review of new surface plasmon resonance technologies ," *Current Opinion in Biotechnology*, vol. 17, pp. 400-405, 2006.
- [27] C. T. Cmpbella and G. Kim, "microscopy and its applications to high-throuput analyses of biomolecular binding events and their kinetics," *Biomaterials*, vol. 2008, pp. 2380-2392, 2007.
- [28] R. L. Richa and D. G: Myszkä, "Survey of the year 2007 commercial

- optical biosensor literature," *Journal of Molecular Recognition* , vol. 21, pp. 355-400, 2008.
- [29] K. E. Sapsford et al., "Fluorescence-based array biosensors for detection of biohazards," *Journal of Applied Microbiology*, vol. 96, pp. 47-58, 2004.
- [30] A. P. Demchenko, "The future of fluorescence sensor Arrays," *Trends in Biotechnology*, vol. 23, no. 9, pp. 456-460, 2005.
- [31] N. Waly. (2011, February) <http://archiv.ub.uni-heidelberg.de/volltextserver/11641/>. [Online]. <http://nbn-resolving.de/urn/resolver.pl?urn=urn:nbn:de:bsz:16-opus-116418>
- [32] K. Sakoda, *Optical Properties of Photonic Crystals*. Berlin-Heidelberg, Germany: Springer-Verlag, 2005.
- [33] A. Herrmann, S. Kuhn, M. Tiegel, and C. Rüssel, "Fluorescence properties of EU³⁺-doped alumino silicate glasses," *Optical Materials*, vol. 37, pp. 293-297, March 2014.
- [34] D. Lewandowski, G. Schroeder, M. Sawczak, and T. Ossowski, "Fluorescence properties of riboflavin-functionalized mesoporous silica SBA-15 and riboflavin solutions in presence of different metal and organic cations," *Journal of Physics and Chemistry of Solids* , vol. 85, pp. 56-61, April 2015.
- [35] M. Oubaha, A. Gorin, C. McDonagh, B. Duffy, and R. Copperwhite,

- "Development of a multianalyte optical sol-gel biosensor for medical diagnostic," *Sensors and Actuators B: Chemical*, vol. 221, pp. 96-103, 2015.
- [36] J. Wang, "Electrochemical biosensors: Towards point-of-care cancer diagnostics," *Biosensors and Bioelectronics*, vol. 21, pp. 1887-1892, 2006.
- [37] M. Pohanka and P Skladal, "Electrochemical biosensors - principles and applications," *Journal of Applied Biomedicine*, vol. 6, pp. 57-64, 2008.
- [38] O. A. Sadik, A. O. Aluoch, and A. Zhou, "Status of biomolecular recognition using electrochemical techniques," *Biosensors and Bioelectronics*, vol. 24, pp. 2749-2765, 2009.
- [39] J. Zhu, X. Liu, X. Wang, X. Huo, and R. Yan, "Preparation of Polyaniline-TiO₂ nanotube composite for the development of electrochemical biosensors," *Sensors and Actuators B: Chemical*, vol. 221, pp. 450-457, 2015.
- [40] Y. Zhang et al., "A reusable piezoelectric immunosensor using antibody-adsorbed magnetic nanocomposite," *Journal of Immunological methods*, vol. 332, no. 1-2, pp. 103-111, 2008.
- [41] T. M. A. Gronewold, "Surface acoustic wave sensors in the bioanalytical field: Recent trend and challenges," *Analytica Chimica Acta*, vol. 603, no. 2, pp. 119-128, 2007.

- [42] Z.P. Yang, X. Liu, C.-J. Zhang, and B.-Z. Liu, "A high performance nonenzymatic piezoelectric sensor based on molecularly imprinted transparent TiO₂ film for detection of urea," *Biosensors and Bioelectronics*, vol. 74, pp. 85-90, 2015.
- [43] M. A.D. Neves, C. Blaszykowski, S. Bokhari, and M. Thompson, "Ultra-high frequency piezoelectric aptasensor for the label-free detection of cocaine," *Biosensors and Bioelectronics*, vol. 72, pp. 383-392, 2015.
- [44] A. Narayanaswamy, J. Mayo, and C. Canetta, "Infrared selective emitters with thin films of polar materials," *Applied Physics Letters*, vol. 104, May 2014.
- [45] J. D. Joannopoulos, R. J. Meade, and J. N. Winn, *Photonic Crystals - Molding the Flow of Light*. Chichester, West Sussex, UK: Princeton University Press, 1995.
- [46] Eli Yablonovitch, "Inhibited Spontaneous Emission in Solid-State Physics and Electronics," *Phys. Rev. Lett.*, vol. 58, no. 20, pp. 2059-2062, May 1987.
- [47] John Sajeev, "Strong localization of photons in certain disordered dielectric superlattices," *Phys. Rev. Lett.*, vol. 58, no. 23, pp. 2486-2489, June 1987.
- [48] R. J. Nicholas and R. S. Tuley, "Thermophotovoltaic (TPV) devices introduction and modelling," in *Functional materials for sustainable energy applications*. Oxford, Cambridge, Philadelphia, New Dehli:

Woodhead Publishing Limited, 2012.

- [49] H. Ye, H. Wang, and Q. Cai, "Two-dimensional VO₂ photonic crystal selective emitter," *Journal of Quantitative Spectroscopy & Radiative Transfer*, vol. 158, pp. 119-126, February 2015.
- [50] M. Garin, D. Hernandez, T. Trifonov, and R. Alcubilla, "Three-dimensional metallo-dielectric selective thermal emitters with high-temperature stability for thermophotovoltaic applications," *Solar Energy Materials & Solar Cells*, vol. 134, pp. 22-28, November 2014.
- [51] M. B. Pushkarsky et al., "High-sensitivity detection of TNT ," *Physical Sciences - Applied Physical Sciences*, vol. 103, no. 52, pp. 19630-19634, Dec. 2006.
- [52] P. Bergese and K. Hamad-Schifferli, *Nanomaterial Interfaces in Biology*. New York, USA: Springer Science+Buisness, 2013.
- [53] L. Kashefi-Kheyraadi, A. Noori, and M. A. Mehrgardi, "Application of Bioconjugated Nanoporous Gold Films in Electrochemical Biosensors," in *Biosensors Nanotechnology*.: Scrivener Publishing LLC, 2014, pp. 345-374.
- [54] D. R. Miller, S.A. Akbar, and P. A. Morris, "Nanoscale metal oxide-based heterojunctions for gas sensing: A review," *Sensors and Actuators B: Chemical*, vol. 2004, pp. 250-272, July 2014.

- [55] Bartelmann et. al., *Theoretische Physik*. Berlin Heidelberg, GER: Springer-Verlag, 2015.
- [56] G. A. Reider, *Photonik*, 3rd ed. Wien, Austria: Springer-Verlag, 2012.
- [57] E. Hecht, *Optics*, 2nd ed. Reading, Mass., USA: Addison-Wesley, 1987.
- [58] G. A. Niklasson, C. G. Granqvist, and O. Hunderi, "Effective medium models for the optical properties of inhomogeneous materials," *applied optics*, vol. 20, pp. 26-30, 1981.
- [59] H. Herwig and A. Moschallski, *Wärmeübertragung*, 3rd ed. Wiesbaden, GER: Springer Verlag, 2014.
- [60] A. M., Schwinger, J. Milton, *Electromagnetic Radiation: Variational Methods, Waveguides and Accelerators*. Berlin Heidelberg, GER: Springer-Verlag, 2006.
- [61] M. F. Modest, *Radiative Heat Transfer*, 2nd ed. San Diego, California, USA: Elsevier Science, 2003.
- [62] Z. M. Zhang, *NANO/MICROSCALE HEAT TRANSFER*. USA: McGraw-Hill Professional, 2007.
- [63] K. Kopitzki and P. Herzog, *Einführung in die Festkörperphysik*, 4th ed. Stuttgart/Leipzig/Wiesbaden, GER: B. G. Teubner GmbH, 2002.
- [64] A. Narayanaswamy and G. Chen, "Surface modes for near field

- thermophotovoltaics," *Applied Physics Letters*, vol. 82, no. 20, pp. 3544-3546, May 2003.
- [65] B. Neuner et al., "Midinfrared Index Sensing of pL-scale Analytes Based on Surface Phonon Polaritons in Silicon Carbide," *The Journal of Physical Chemistry C*, vol. 114, no. 16, pp. 7489-7491, March 2010.
- [66] V. A. Parsegian, *Van der Waals Forces - A Handbook for Biologists, Chemists, Engineers, and Physicists*. New York, New York, USA: Cambridge University Press, 2006.
- [67] A. Ghanekar, L. Lin, J. W.: Sun, H. W. Su, and Y. Zheng, "Role of nanoparticles in wavelength selectivity of multilayered structures in the far-field and near-field regimes," *Applied Physics Letters*, pp. 1-5, 2015.
- [68] U. Kreibig and M. Vollmer, *Optical Properties of Metal Clusters*. Berlin- Heidelberg, GER: Springer-Verlag, 1995.
- [69] P. B. Johnson and R. W. Christy, "Optical Constants of the Noble Metals," *Physical Review B*, vol. 6, no. 12, pp. 4370-4379, December 1972.
- [70] W. C. Chew, *WAVES AND FIELDS IN INHOMOGENEOUS MEDIA*. New York, USA: IEEE PRESS, 1995.
- [71] Inc. The MathWorks. (2015) MathWorks. [Online]. HYPERLINK "mathworks.com" mathworks.com
- [72] B. Hudson and R. Jacobs, "The Ultraviolet Transitions of the

- Ethidium Cation," *Biopolymers*, vol. 14, pp. 1309-1312, 1975.
- [73] S. Biswas, S. C. Bhattacharya, B. B. Bhowmik, and S. P. Moulik, "Absorption and Emission Characteristics of 7-Hydroxycoumarin and 1-Hydroxypyrene-3,6,8-trisulfonate in Water/Oil Microemulsion with Reference to the Determination of the Interfacial and Bulk pH of the Water pool," *Journal of Colloid and Interface Science*, vol. 244, pp. 145-153, 2001.
- [74] M. L. S. Albuquerque et al., "Characterization of Buriti (*Mauritia flexuosa* L.) Oil by Absorption and Emission Spectroscopies," *J. Braz. Chem. Soc*, vol. 16, no. 6A, pp. 1113-1117, 2005.
- [75] F.J. Jongeneelen, R.B.M. Anzion, and P.Th. Henderson, "Determination of hydroxylated metabolites of polycyclic aromatic hydrocarbons in urine," *Journal of Chromatography*, vol. 413, pp. 227-232, 1987.
- [76] M. Simsikova, J. Cechal, A. Zorkovska, and M. Antalík, "Preparation of CuO/ZnO nanocomposite and its application as a cysteine/homocysteine colorimetric and fluorescence detector," *Colloids and Surfaces B: Biointerfaces*, vol. 123, pp. 951-958, 2014.
- [77] S. Wray et al., "Characterization of the near infrared absorption spectra of cytochrome aa₃ and haemoglobin for the non-invasive monitoring of cerebral oxygenation," *Biochimica et Biophysica Acta*, vol. 933, pp. 184-192, 1988.

- [78] C. A. Merlic and B. C. Fam. (2000, June) WebSpectra. [Online].
HYPERLINK "http://www.chem.ucla.edu/~webspectra/index.html"
<http://www.chem.ucla.edu/~webspectra/index.html>
- [79] I. Nakagawa and T. Shimanouchi, "Infrared absorption spectra of aquo complexes and the nature of co-ordination bonds," *Spectrochimica Acta*, vol. 20, pp. 420-439, 1964.
- [80] K. Raman, T. R. Srinivasa Murthy, and G. M. Hegde, "Fabrication of Refractive Index Tunable Polydimethylsiloxane Photonic Crystals for Biosensor Application," *Physics Procedia*, vol. 19, pp. 146-151, 2011.
- [81] MIDWEST TUNGSTEN SERVICE. tungsten.com. [Online].
HYPERLINK "http://www.tungsten.com/wp-content/uploads/2014/03/tipsbeam.pdf"
<http://www.tungsten.com/wp-content/uploads/2014/03/tipsbeam.pdf>
- [82] S. S. Lau, "Epitaxial Growth of Silicon Structures - Thermal, Laser-, and Electron-Beam-Induced ," in *Preparation and Properties of Thin Films*. New York, London: Academic Press, 1982.
- [83] A. Folch, J. Tejada, C. H. Peters, and M. S. Wrighton, "Electron Beam deposition of gold nanostructures in a reactive environment," *Applied Physics Letters*, vol. 66, no. 16, pp. 2080-2082, January 1995.
- [84] F. Zabihi, Y. Xie, S. Gao, and M. Eslamian, "Morphology, conductivity, and wetting characteristics of PEDOT:SS thin films deposited by spin and spray coating," *Applied Surface Science*, vol. 338,

pp. 163-177, February 2015.

- [85] A. Dols-Perez, L. Fumagalli, A. C. Simonsen, and G. Gomila, "Ultrathin Spin-Coated Dioleoylphosphatidylcholine Lipid Layers in Dry Conditions: A Combined Atomic Force Microscopy and Nanomechanical Study," *American Chemical Society*, vol. 27, no. 21, pp. 13165-13172, September 2011.
- [86] S. Panigrahi, S. Waugh, S. K. Rout, A. K. Hassan, and A. K. Ray, "Study of Spin Coated Organic Thin Film Under Spectrophotometer," *Indian Journal of Physics*, vol. 78, no. 8, pp. 823-826, 2004.
- [87] A. A. Christy, Y. Ozaki, and V. G. Gregoriou, "Modern Fourier Transform Infrared Spectroscopy," *Comprehensive Analytical Chemistry*, vol. 35, 2001.
- [88] B. C. Smith, *Fundamentals of Fourier Transform Infrared Spectroscopy*. Boca Ranton, Florida, USA: Taylor and Francis Group, 2001.
- [89] Bruker Optics. (2010) [bruker.com](https://www.bruker.com/fileadmin/user_upload/8-PDF-Docs/Optical%20Spectroscopy/FT-IR/VERTEX/AN/AN99_SolarThermalMaterials_EN.pdf). [Online]. HYPERLINK "https://www.bruker.com/fileadmin/user_upload/8-PDF-Docs/Optical Spectroscopy/FT-IR/VERTEX/AN/AN99_SolarThermalMaterials_EN.pdf" https://www.bruker.com/fileadmin/user_upload/8-PDF-Docs/Optical Spectroscopy/FT-IR/VERTEX/AN/AN99_SolarThermalMaterials_EN.pdf

- [90] P. A. Tipler and G. Mosca, *Physik*, 7th ed. Berlin Heidelberg, Deutschland: Wagner, J., 2015.
- [91] Y. S. Touloukain and D. P. DeWitt, *THERMAL RADIATIVE PROPERTIES - Metallic Elements and Alloys*. New York, USA: Springer Science+Business Media, 1970, vol. 7.
- [92] Misza Kalechman, *Practical MATLAB basics for engineers*. Boca Raton, FL, USA: CRC Press, 2007.
- [93] G. K. Knopf and A. S. Bassi, *Smart Biosensor Technology*. Rochester, New York, USA: CRC Press, 2007.
- [94] E. D. Paik, *Handbook of Optical Constants of Solids*. San Diego, USA: Academic Press, 1998.
- [95] A. D. Rakic, A. B. Djuricic, J. M. Elazar, and M.L. Majewski, "Optical properties of metallic film for vertical-cavity optoelectronic devices," *Optical Physics*, vol. 37, no. 22, pp. 5271-5283, August 1998.
- [96] M. del Valle and A. Bonanni, "Impedimetric DNA Biosensors Based on Nanomaterials," in *Biosensors Nanotechnology.*, 2014, pp. 81-110.
- [97] M. Stevanovic, "Assembly of Polymers/Metal Nanoparticles and Their Applications as Medical Devices," in *Biosensors Nanotechnology.:* Scrivener Publishing, 2014, pp. 37-62.
- [98] Ü. Anik, "Gold Nanoparticle-Based Electrochemical Biosensors for Medical Applications," in *Biosensors Nanotechnology.:* Scrivener

Publishing LLC, 2014, pp. 63-80.

- [99] A. H. Nayfeh, "Wave Propagation in Layered Anisotropic Media with Applications to composites," *North-Holland Series in Applied Mathematics and Mechanics*, vol. 29, pp. 1-332, 1995.
- [100] X. Huang, I. H. El-Sayed, W. Qian, and M. A. El-Sayed, "Cancer Cell Imaging and Photothermal Therapy in the Near-Infrared Region by using Gold Nanorods," *Journal of American Chemical Society*, vol. 128, pp. 2115-2120, January 2006.
- [101] Helmholtz Zentrum Berlin. (2015, February) [helmholtz-berlin.de](http://www.helmholtz-berlin.de).
[Online]. HYPERLINK "http://www.helmholtz-berlin.de/forschung/oe/ee/si-pv/verfahren/abscheideverfahren/elektronenstrahlverdampfung_de.html"
http://www.helmholtz-berlin.de/forschung/oe/ee/si-pv/verfahren/abscheideverfahren/elektronenstrahlverdampfung_de.html